catalysts

MDPI

Article

Synthesis of Low-Cost CuSn Catalysts for the Electrochemical Conversion of CO_2 and Water to Formate and Syngas

Luis Gerardo Navarro-Tovar [1,*], Mayra Sareth Tovar-Oliva [1], Sebastián Murcia-López [2,†] and Ignacio Tudela [1,*]

[1] School of Engineering, Institute for Materials and Processes, Edinburgh Electrochemical Engineering Group (e3 Group), The University of Edinburgh, Sanderson Building, Robert Stevenson Road, Edinburgh EH9 3FB, UK
[2] Catalonia Institute for Energy Research (IREC), Jardins de les Dones de Negre 1, 08930 Sant Adrià de Besòs, Catalonia, Spain
* Correspondence: l.g.navarro-tovar@sms.ed.ac.uk (L.G.N.-T.); ignacio.tudela@ed.ac.uk (I.T.)
† Current address: Catalan Institute of Nanoscience and Nanotechnology (ICN2), Edifici ICN2, UAB Campus, 08193 Bellaterra, Barcelona, Spain.

Abstract

The electrochemical reduction of CO_2 offers a sustainable approach to transforming carbon dioxide into value-added products when powered by renewable energy. However, current electrocatalysts lack efficiency and selectivity, hindering commercial application. Combining tin's high formate selectivity with copper's ability to reduce CO_2 via COOH* pathway offers a promising strategy. This synergy mitigates copper's low selectivity, providing a cost-effective catalyst with enhanced performance over pure Sn-based systems. This work investigates CuSn bimetallic electrocatalysts synthesised by scalable electrodeposition onto gas diffusion layers to boost formate production. Catalytic performance and cell potential were evaluated at current densities ranging from 50 to 200 mA cm^{-2} and varying Sn compositions. Catalysts with Sn content below 4% predominantly formed CO and H_2, but smaller particles and improved metal dispersion increased formate production. A catalyst containing 12% Sn achieved a maximum faradaic efficiency (FE) of 52% at 50 mA cm^{-2} with an *iR*-corrected potential of −0.56 V vs. SHE. At 200 mA cm^{-2}, it exhibited a 30% FE for formate, along with 31% FE for CO and 9.3% FE for H_2, while other gases contributed to less than 4% FE, indicating potential as syngas feedstock. Higher Sn content, combined with smaller, well-distributed particles, effectively suppressed H_2, CO, and other by-products, highlighting a strong dependence of FE on Sn content and bimetallic distribution, demonstrating compositional tuning importance via electrodeposition.

Keywords: CO_2 electrolysis; electrocatalysis; electrodeposition; copper; tin; gas diffusion electrodes

Check for updates

Academic Editor: Xiaohong Yang

Received: 30 September 2025
Revised: 15 December 2025
Accepted: 5 January 2026
Published: 16 March 2026

Copyright: © 2026 by the authors. Licensee MDPI, Basel, Switzerland. This article is an open access article distributed under the terms and conditions of the Creative Commons Attribution (CC BY) license.

1. Introduction

Greenhouse gases (GHGs) trap heat in the Earth's atmosphere, resulting in an increase in the average temperature of our planet. Both natural processes and human activities contribute to GHG emissions, with key gases including CO_2, methane and nitrous oxide, among others [1]. Rising GHG levels in the atmosphere intensify air pollution, affect ecosystems and impact human life by increasing both the frequency and severity of extreme weather events and or even increasing respiratory diseases [2–4].

Anthropogenic activities have disrupted the natural carbon cycle, causing CO_2 emissions and atmospheric concentrations to reach record highs annually since instrumental

measurements have started to be reported [5–7]. Among all industrial sectors, the chemical industry consumes the most energy and is the third-largest contributor to direct CO_2 emissions, exceeding 6% globally [8–11]. Clean renewable energy technologies have grown significantly since 2019, supported by strong government policies, which have contributed to slowing the growth of global CO_2 emissions (mitigating a potential tripling of emissions) [9,12]. In this regard, despite a 1.1% rise in emissions driven by energy demand, the deployment of clean renewable energy technologies, including a 360% increase in electrolyser capacity for hydrogen production, mainly in China, contributed to avoid a far more substantial increase in 2023 [9,12]. These efforts have indeed contributed to the slowest emissions growth since the Great Depression, at about 0.5% per year, despite GDP growth of 1.7% [9,12]. However, this progress alone is not sufficient to decarbonise energy-intensive sectors like the chemical industry.

Given the scale of emissions from the chemical industry, use of renewable energy alone in industrial processes seems insufficient [13,14], as achieving meaningful decarbonisation in this sector will require fundamental shifts in feedstock, processes and carbon management strategies [15]. Strategies to reduce emissions can be grouped into three categories [16]: (1) reduction at the source focused on decarbonisation while maintaining economic growth [17,18], (2) carbon capture followed by sequestration (CCS) aiming at preventing CO_2 release into the atmosphere while accepting continued emisions [19–21], and (3) capture followed by utilisation (CCU) [22]. CCU is particularly attractive, as it transforms CO_2 into valuable chemicals. Therefore, captured CO_2 can be valorised as a sustainable energy source or raw material, rather than merely as a pollutant.

CO_2, with C in its +4 oxidation state, is the most oxidised form of carbon and requires a transference of electrons for its valorisation, a process known as CO_2 reduction (CO_2R) [23]. This differs from the thermodinamically favoured mineral carbonation, where CO_2 binds into stable carbonates with little energy input [24]. In contrast, CO_2R requires energy to overcome its negative free energy of formation, achievable through (a) chemical [24–30], (b) photochemical [31–34], (c) biochemical [35–37], and (d) electrochemical methods [38–52], and (e) combinations of some or all of these techniques. Each method has its own challenges affecting commercial viability, in addition to CO_2's inherent kinetic and thermodynamic stability [28,40,53]. However, CO_2R using captured CO_2 and electricity from renewable energy sources under ambient conditions offers a sustainable route forward. The possibility of producing high-value carbon-based compounds such as ethylene [41–44] and formate [45–47], or fuels such as methanol [48–50] and ethanol [51], rather than simply sequestering CO_2 underground, further supports this idea. Among these, formate is an attractive product from CO_2R due to its simple two-electron, two-proton formation pathway. Several transition and post-transition metals such as Pb, Hg, Tl, In, Sn, Cd, and Bi can be classified as formate producers catalysts [16]. However, only In, Sn, and Bi are suitable candidates because of their relatively lower toxicity and environmental impact.

As of July 2025, market data indicate that Sn is the most economical option among the three; according to the London Metal Exchange, the average price of tin was approximately \$15 USD per kilogram, making it at least 20 times cheaper than In (\$330 USD per kg) and Bi (\$380 USD per kg) [54–56]. In Sn, CO_2 weakly adsorbs and forms formate without C–O bond cleavage, making it the second most accessible product kinetically after CO [29]. Formic acid also offers a high value of \$0.015 USD/mole of electron consumed, second only to CO [53]. However, pure Sn typically exhibits high faradaic efficiency (FE) for formate only at low current densities (*i*) [16,57], limiting its industrial applicability. Introducing a second metal to form a bimetallic catalyst enables synergistic effects [46]. Copper is a promising catalyst due to its high conductivity and selective CO binding [58,59]. While it adsorbs hydrogen at CO_2 reduction potentials, it does not become fully covered, though

the hydrogen evolution reaction (HER) remains a competing reaction [60]. Incorporating Sn enhances selectivity by strongly stabilizing HCOO* intermediates and weakly binding H*, thereby favoring formate formation over competing HER [60–62].

Achieving optimal performance in CO_2R catalysts requires careful tuning of surface structure and particle size [63–65]. However, conventional post-synthesis application methods, such as spraying or brushing onto electrode substrates, often introduce variability due to procedural inconsistencies and dependence on operator skill [66]. The resulting non-uniform catalyst layers may lead to poor electrochemical performance, including hotspots, uneven current distribution and accelerated material failure [67]. Electrodeposition offers a direct and efficient route to synthesise catalysts directly onto conductive supports, ensuring strong electrical connectivity and minimising interfacial resistance [66]. Unlike traditional ex-situ techniques, this method streamlines fabrication and allows rapid deposition of a wide range of transition and post-transition metals relevant to CO_2RR. Moreover, electrodeposition parameters, such as current density, applied potential, deposition time, and agitation, can be finely tuned to tailor the surface structure, particle size, morphology, composition, and ultimately, the catalytic performance and product selectivity of the resulting CO_2 electrocatalysts [66,68,69]. In the case of CuSn, it can operate at room temperature without the need for high-temperature processes lowering energy demands and avoiding thermal stress on the substrate [70–72].

While most studies on electrodeposited CuSn catalysts for CO_2RR were conducted at current densities below 50 mA cm^{-2} applied during the electrolysis experiments, industrially viable processes require a current density at least four times higher. Therefore, the impact of electrodeposition parameters on catalyst quality and performance under these more demanding conditions remains underexplored or limited to small-scale electrodes and short operation times. For instance, Li et al. [73] achieved 82% FE for formate at a current density of 181 mA cm^{-2}. However, the electrode area was only 1 cm^2, and the plating required a charge of 80 C cm^{-2} along with an intensive substrate pretreatment.

In this study, we systematically investigate how electrodeposition parameters influence morphology characteristics such as composition and particle size, and performance of CuSn bimetallic catalysts for CO_2 electroreduction, with a focus on optimising conditions for selective formate and syngas production for flow cell configurations with a 5 cm^2 geometric active area. We demonstrate that careful compositional tuning via electrodeposition significantly impacts product selectivity in CO_2RR; catalysts with Sn content below 4% predominantly produced CO and H_2, whereas increasing the Sn content and achieving better metal dispersion favoured formate production. Notably, a catalyst containing 12% of Sn reached a maximum FE of 52% for formate at 50 mA cm^{-2} at an *iR*-corrected potential of −0.56 V vs. SHE, achieving a 30% FE for formate at 200 mA cm^{-2}, alongside 31% FE for CO and 9.3% FE for H_2. The minor formation of other gaseous products (FE < 4%) indicates promise for syngas applications. These results confirm that increasing Sn content, while optimising particle size and distribution, suppresses undesired by-products and enhances formate selectivity.

2. Results and Discussion

2.1. Optimisation of Catalyst Synthesis via Electrodeposition

Careful optimisation of electroplating bath composition and key process parameters such as additives, pH, temperature, applied current density or the total charge passed is essential for tailoring the morphology, mechanical strength and physicochemical characteristics of electrodeposited materials [74]. Following prior work on the electrodeposition of pure Cu catalysts for CO_2RR to mainly ethylene and ethanol [38], we optimised the electrodeposition of bimetallic CuSn on commercial GDLs by tuning bath composition,

current density and charge passed to ensure uniform and reproducible catalyst deposition. For this purpose, we comprehensively evaluated a range of process conditions, including Cu, Sn and MSA concentrations, at five different current densities (8, 10, 15, 20 and 30 mA cm^{-2}) and charge passed (1, 2 and 4 C cm^{-2}) to identify the optimal parameters for the reproducible electrodeposition of CuSn electrodeposition on commercial carbon-based GDLs. The optimisation process was guided by the following criteria:

1. Acid selection: In our previous work [38], sulfuric acid was used as the acidic component in electrodeposition baths. Despite its effectiveness, it presents challenges such as strong oxidising behaviour, which can promote the unwanted oxidation of Sn^{2+} to Sn^{4+} in the bath, significantly compromising the stability of the bath and its lifespan in industrial settings; MSA's weaker oxidising nature enhances bath stability, making it a more suitable electrolyte for the reliable electrodeposition of CuSn catalysts [70–72]. In addition, MSA generally presents superior metal salt solubility, lower corrosivity, and some environmental advantages such as low toxicity, biodegradability, and simplified effluent treatment [75,76].
2. Bath composition: Stepwise trials were conducted to optimise bath composition for adhesion, morphology and Sn content. Initial trials conducted at pH 1 resulted in CuSn catalysts that either were missing or adhered poorly to the GDL (Figure 1). Increasing the concentration of MSA to 1.22 M facilitated the electrodeposition of CuSn catalysts, but with very low Sn content (<2%). Decreasing Cu and increasing Sn content in the bath did indeed lead to an improvement in the incorporation of Sn in the catalysts structures, although it also resulted in salt precipitation from the bath, likely caused by limited acid buffering capacity and the oxidation of Sn^{2+} to Sn^{4+}. A $[Cu^{2+}]/[Sn^{2+}]$ molar ratio of 10 marked the onset for enhanced Sn content; further reducing the concentration of Cu in the bath while increasing MSA content from 1.22 M to 1.53 M and keeping the same $[Cu^{2+}]/[Sn^{2+}]$ molar ratio did lead to higher Sn incorporation than its lower-acid counterpart. Increasing the acidity was critical in this case, as salt precipitation from the electrolyte was again observed in those conditions when the concentration of MSA was 1.22 M, whereas the higher MSA concentration resulted in a more deposition process, establishing a baseline for further optimisation. $[Cu^{2+}]/[Sn^{2+}]$ molar ratios of 10, 5, 2, and 1 were subsequently selected for further evaluation.
3. Current density: SEM analysis was conducted on CuSn samples with successful deposition and no precipitation under the bath conditions depicted in Figure 1; the corresponding results are displayed in Figures A4–A8 available in the Appendix A. At 8 mA cm^{-2}, the electrodeposited catalysts generally presented a poor, uneven distribution, whereas increasing the current density during the electrodeposition progressively led to a more uniform distribution of catalysts across the surface of the GDL. The reason for this is the early nucleation occurring at the beginning of the electrodeposition process, combined with a more uneven distribution of current density at lower electrode overpotentials (see thorough discussion on the topic in previous work by the authors [38]). Overall, a generally uniform distribution of catalysts with similar morphologies was observed at current densities of $\geq$10 mA cm^{-2} with varying amounts of Sn, which is why current densities of 10, 20 and 30 mA cm^{-2} were selected for further investigation.
4. Catalyst loading: Several catalyst loadings worth 1, 2 and 4 C cm^{-2} were evaluated in electroplating baths with different Cu^{2+} concentrations (0.1 or 0.05 M) and $[Cu^{2+}]/[Sn^{2+}]$ molar ratios of 10, 5, 2, and 1 at several current densities (10, 20 and 30 mA cm^{-2}) where the concentration of MSA was maintained at 1.53 M (Figure 2). For catalyst loadings worth 1 C cm^{-2}, deposits were only noticeable at the lowest

and highest $[Cu^{2+}]/[Sn^{2+}]$ molar ratios (1 and 10, respectively), although coverage was uneven with a poor catalyst distribution in both cases. This is fairly common when catalysts are electrodeposited over porous 3D supports [77] like the GDLs used in this study, with the cause likely being the nucleation of Cu in sulfate baths [38]. Increasing the catalyst loading to 2 and 4 C cm^{-2} resulted in GDEs with more noticeable and evenly distributed CuSn catalysts better distributed visually due to the current distribution becoming more uniform as more catalyst is being deposited. In fact, the GDEs with a catalyst loading worth 4 C cm^{-2} presented a nearly continuous and relatively thick 'thin' CuSn film with different surface textures and changes in colour (grey in this case), particularly at lower $[Cu^{2+}]/[Sn^{2+}]$ molar ratios. This likely reflects a shift in the dominant metal being electrodeposited: Cu^{2+}, with a more positive reduction potential, will deposit faster than Sn^{2+}, which has a more negative reduction potential (GDEs with catalyst loadings of 1 and 2 C cm^{-2}); nevertheless, as the electrodeposition process continues and the concentration of Cu^{2+} near the electrode progressively decreases at a faster rate than that of Sn^{2+}, the $[Cu^{2+}]/[Sn^{2+}]$ at the electrode/electrolyte interface is decreased in practice, leading to an increase in Sn co-deposition. Overall, increasing the applied charge from 1 to 4 C cm^{-2} resulted in GDEs that went from presenting insufficient and non-uniform catalyst coverage at low catalyst loadings (especially at low current densities) to exhibiting fully covered surfaces with 'taller/thicker' catalyst structures at high catalyst loadings (especially at high current densities, where continuous films could be clearly observed), as confirmed by SEM analysis (Figures A9–A12). One could initially be tempted to select the GDEs with the highest catalyst loadings as the most suitable option for further analysis; however, too much coverage of the surface of the GDEs, especially with semi-continuous, non-porous films, can lead to partial blocking of the pores within the surface of the GDL, impeding CO_2 transport to the catalyst–electrolyte interface, shifting selectivity toward the hydrogen evolution reaction (HER) and increasing the cell potential, impacting the overall electrochemical performance [38,60].

To gain deeper insight into the CuSn electrodeposition system, a cyclic voltammetry (CV) study was carried out in GDLs subjected to the identical pre-treatment used to prepare the GDEs fabricated during this study to ensure that the electrochemical response recorded during the CVs closely mirrors the behaviour of the actual electrodeposition process. Figure 3 displays the electrochemical response of the Cu–Sn system in 1.53 M MSA at 1 mV s^{-1} without the additive (DAT). A well-defined cathodic peak (Peak A) appears at –0.02 V for the Cu^{2+} bath and at –0.11 V vs. Ag/AgCl for the bath containing both Cu^{2+} and Sn^{2+}, corresponding to the reduction of Cu^{2+} to metallic Cu [38,72]. This is followed by a second cathodic peak (Peak B) at −0.44 V vs. Ag/AgCl for the pure Sn^{2+} bath and at −0.49 V vs. Ag/AgCl for the mixed Cu^{2+}–Sn^{2+} bath, which can be assigned to the reduction of Sn^{2+} to metallic Sn [72,78]. A sharp rise in current at potentials more negative than −0.5 V vs. Ag/AgCl corresponds to HER. On the reverse scan, two anodic peaks (Peak C) are observed: −0.33 V vs. Ag/AgCl for the Sn^{2+} bath and −0.40 V vs. Ag/AgCl for the mixed Cu^{2+}–Sn^{2+} bath, which can be attributed to Sn oxidation to Sn^{2+} [72,78]. A second anodic peak (Peak D) is visible near 0.20 V vs. Ag/AgCl for the Cu^{2+} bath and at 0.16 V vs. Ag/AgCl for the mixed Cu^{2+}–Sn^{2+} bath, corresponding to the oxidation of Cu to Cu^{2+}. Overall, this confirms why, at the beginning of the electrodeposition process, Cu^{2+} is more likely to reduce, resulting to higher Cu content in the catalyst, whereas as the electrodeposition continues and the concentration of Cu^{2+} decreases at the electrode/electrolyte interface, more Sn^{2+} is reduced and the Sn content in the catalysts progressively increases.

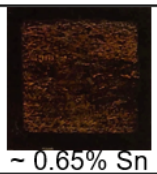
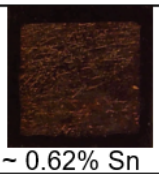
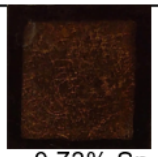
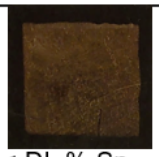
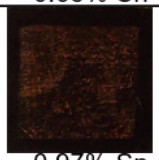
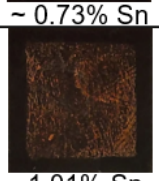
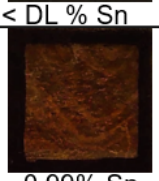
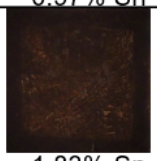
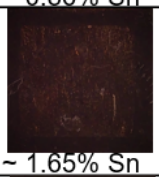
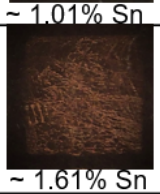
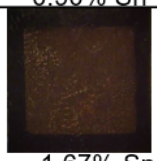
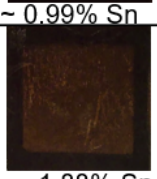
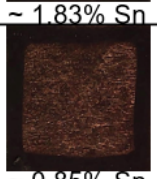
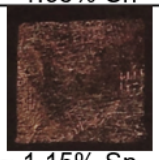
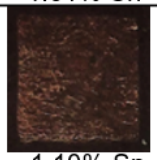
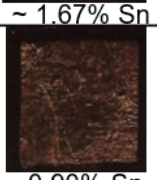
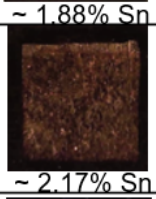
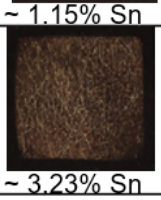
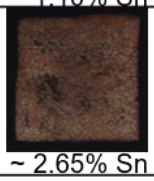
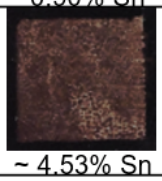
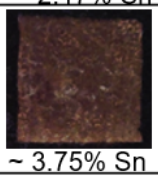
[Cu] (M)	[Sn] (M)	[Cu]/[Sn] (M/M)	MSA [M]	8 mA cm^{-2}	10 mA cm^{-2}	15 mA cm^{-2}	20 mA cm^{-2}	30 mA cm^{-2}
0.2	0.025	8	pH 1	Bad Deposit (Lack of Adhesion)				
0.1	0.050	5	pH 1	Did not plate, overpotential and unstable electrolyte				
0.05	0.050	1	pH 1	Did not plate, overpotential and unstable electrolyte				
0.2	0.005	40	1.22	 ~ 0.65% Sn	 ~ 0.62% Sn	 ~ 0.73% Sn	 ~ 0.20% Sn	 < DL % Sn
0.2	0.010	20	1.22	 ~ 0.97% Sn	 ~ 0.86% Sn	 ~ 1.01% Sn	 ~ 0.90% Sn	 ~ 0.99% Sn
0.2	0.020	10	1.22	 ~ 1.83% Sn	 ~ 1.65% Sn	 ~ 1.61% Sn	 ~ 1.67% Sn	 ~ 1.88% Sn
0.1	0.010	10	1.22	 ~ 0.85% Sn	 ~ 1.15% Sn	 ~ 1.10% Sn	 ~ 0.90% Sn	 ~ 2.17% Sn
0.1	0.010	10	1.53	 ~ 1.80% Sn	 ~ 3.23% Sn	 ~ 2.65% Sn	 ~ 4.53% Sn	 ~ 3.75% Sn
0.05	0.010	5	1.22	Precipitation during synthesis required increasing [MSA] to 1.53 M to achieve a good deposit. This bath composition served as the initial basis for further optimisation.				
0.05	0.025	2	1.22					
0.05	0.050	1	1.22					

Figure 1. Visual appearance of GDEs after electrodeposition of CuSn catalysts on carbon-based GDLs from a MSA electrolyte under different process parameters. Catalyst load = 2 C cm^{-2}.

Figure 4 displays the electrochemical response of the Cu–Sn system in 1.53 M MSA at 1 mV s^{-1} with the additive DAT. For the Cu^{2+} bath, the cathodic reduction peak (Peak *A*′) appeared at –0.06 V vs. Ag/AgCl and at –0.17 V vs. Ag/AgCl for the mixed Cu^{2+}–Sn^{2+} bath, representing shifts of approximately –0.04 V vs. Ag/AgCl and –0.06 V vs. Ag/AgCl, respectively, to more negative potentials compared with the additive-free system. In the Sn^{2+} bath, the cathodic peak (Peak *B*′) was observed at –0.45 V vs. Ag/AgCl, while in the mixed Cu^{2+}–Sn^{2+} bath the same peak was noticed near –0.50 V, similar to the behaviour previously reported without DAT. On the reverse scan, anodic peaks (Peak *C*′) associated with Sn^{2+} oxidation were found at –0.32 V vs. Ag/AgCl for the Sn^{2+} bath and at –0.41 V vs. Ag/AgCl for the mixed Cu^{2+}–Sn^{2+} bath, while Cu oxidation peaks (Peak *D*′) appeared at 0.18 V vs. Ag/AgCl for the Cu^{2+} bath and 0.17 V vs. Ag/AgCl for the mixed Cu^{2+}–Sn^{2+} bath. These anodic features remain close to those without the additive, though small shifts are evident, probably due to the complexing nature of the additive.

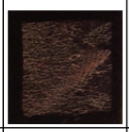
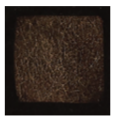
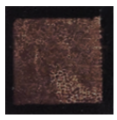
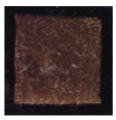
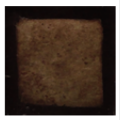
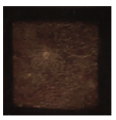
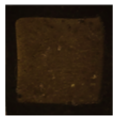
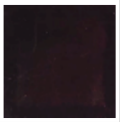
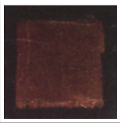
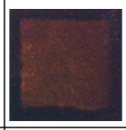
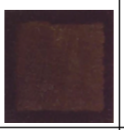
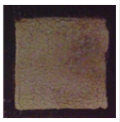
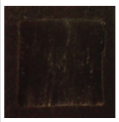
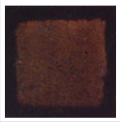
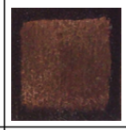
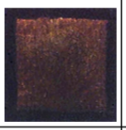
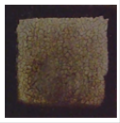
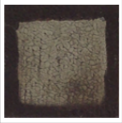
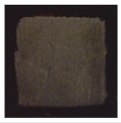
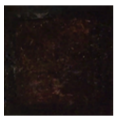
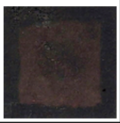
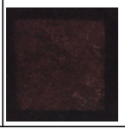
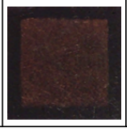
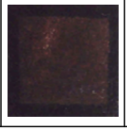
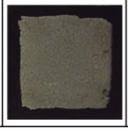
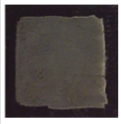
[Sn] (M)	[Cu]/[Sn] (M)	1 C cm^{-2}			2 C cm^{-2}			4 C cm^{-2}		
		10 mA cm^{-2}	20 mA cm^{-2}	30 mA cm^{-2}	10 mA cm^{-2}	20 mA cm^{-2}	30 mA cm^{-2}	10 mA cm^{-2}	20 mA cm^{-2}	30 mA cm^{-2}
0.010	10									
0.010	5									
0.025	2									
0.050	1									

Figure 2. Visual appearance of GDEs after electrodeposition of different CuSn catalyst loadings (1, 2 and 4 C cm^{-2}) under various current densities (10, 20, and 30 mA cm^{-2}) on carbon-based GDLs from a 1.53 M MSA electrolyte with varying [Cu^{2+}]/[Sn^{2+}] molar ratios (10, 5, 2, and 1).

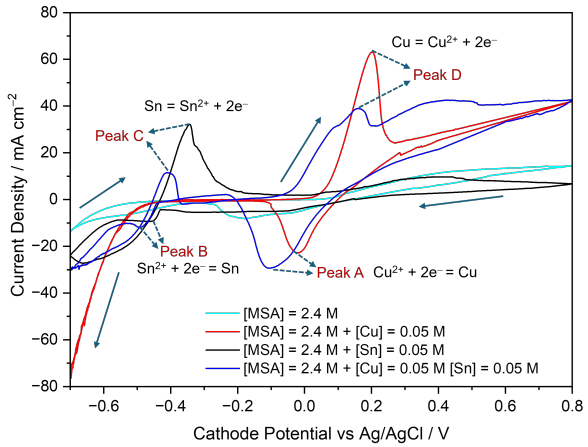


Figure 3. Cyclic voltammetries conducted over a carbonaceous GDL immersed in an MSA electrolyte with no additive (DAT). The scan rate was 1 mV s^{-1}.

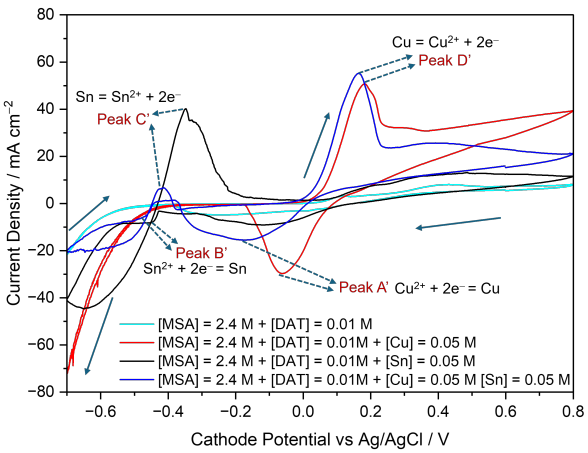


Figure 4. Cyclic voltammetries conducted over a carbonaceous GDL immersed in an MSA electrolyte with additive (DAT). The scan rate was 1 mV s^{-1}.

To better compare the Cu–Sn system with and without the additive, Figure 5 displays the CVs with and without DAT extracted from Figures 3 and 4 commented above. The presence of DAT seemed to decrease, to some extent, the current density of the Cu cathodic peak while enhancing and sharpening the anodic response, indicating improved dissolution behaviour of the Cu deposit while shifting, to some extent, the cathodic peak while reducing the kinetics of the Cu deposition process. On the other hand, the deposition of Sn seemed to be less affected by the presence of the additive, indicating that the addition of DAT may selectively modify Cu nucleation and growth without significantly affecting the electrodepostion of Sn. At potentials more negative than −0.6 V vs. Ag/AgCl, the overall current was suppressed in the DAT-containing bath, consistent with partial inhibition of HER [79]. The results highlight the role of DAT in moderating Cu deposition and enhancing reversibility during the Cu deposition–dissolution cycle. The large potential gap between Cu and Sn reduction implies that CuSn alloy co-deposition occurs only at sufficiently negative potentials to drive both reduction processes simultaneously (i.e., below –0.40 V vs. Ag/AgCl). However, by reducing to some extent the kinetics of the Cu deposition process, DAT indeed facilitates the electrodeposition of CuSn catalysts with higher Sn content.

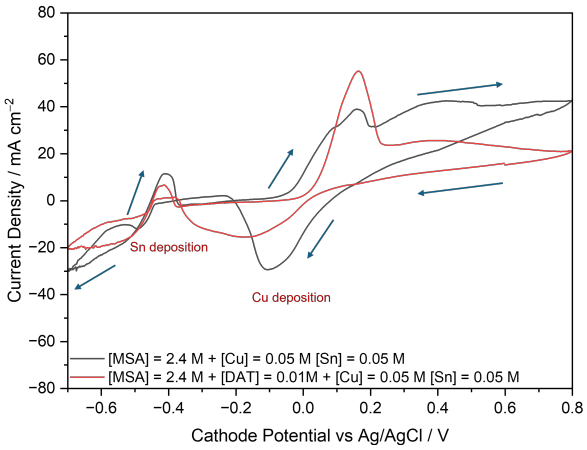


Figure 5. Cyclic voltammetries conducted over a carbonaceous GDL immersed in an MSA electrolyte with and without additive (DAT). The scan rate was 1 mV s^{-1}.

2.2. Catalyst Characterisation

The optimisation of electrodeposition parameters discussed above established that a catalyst loading worth 2 C cm^{-2}, combined with an acid concentration of 1.53 M MSA, provided the most consistent and uniform CuSn deposits, particularly at [Cu^{2+}]/[Sn^{2+}] molar ratios below 10. Based on these results, three representative molar ratios of 10, 5, and 1 were chosen for further characterisation by SEM, EDS, and electrochemical surface area (ECSA) analysis, as they span the transition from Sn-poor to Sn-rich catalysts.

Table 1 summarises the qualitative characteristics of the resulting deposits. This comparison offers a clear framework for identifying conditions that yield low (L), optimal (O), or heavy (H) catalysts structures/films across different synthesis windows. At low catalyst loadings (1 C cm^{-2}), catalysts were generally sparse and poorly distributed, categorised as low coverage (L) across all ratios and current densities, confirming that insufficient applied charge limits catalysts distribution regardless of bath composition. Conversely, at high charges (4 C cm^{-2}), heavy (H) deposits formed, particularly at lower [Cu^{2+}]/[Sn^{2+}] ratios, suggesting that extended plating favours thick, continuous layers that can compromise gas diffusion properties. In contrast, intermediate deposition at 2 C cm^{-2} consistently resulted in an optimal (O) distribution of catalysts, characterised by uniform coverage and strong adhesion. This observation was robust across the three molar ratios and deposition currents

of 10–30 mA cm^{-2}, emphasising the importance of balancing charge and current density to avoid both under- and over-deposition. Therefore, as previously suggested, a charge of 2 C cm^{-2} provided the most reliable catalyst load for generating uniformly distributed CuSn catalysts, ensuring sufficient Sn incorporation without triggering excessive growth or structural defects, and was thus selected as the baseline for the detailed structural and electrochemical analyses presented in the following subsections.

Table 1. Deposit characteristics of CuSn catalysts with different loadings electrodeposited over carbonaceous GDLs from a MSA bath with different $[Cu^{2+}]/[Sn^{2+}]$ molar ratios under various current densities.

Molar ratio $[Cu^{2+}]/[Sn^{2+}]$		10			5			1	
Catalyst loading (C cm^{-2})	1	2	4	1	2	4	1	2	4
Current density (mA cm^{-2})	**Deposit characteristics**								
10	L	O	H	L	O	H	L	O	H
20	L	O	H	L	O	H	L	O	H
30	L	O	H	L	O	H	L	O	H

Notes: L = Low; O = Optimal; H = Heavy.

2.2.1. Catalyst Composition

Figure 6 displays the Sn content in CuSn catalysts electrodeposited in an electrolyte containing 1.53 M MSA with varying $[Cu^{2+}]/[Sn^{2+}]$ molar ratios (1, 5 and 10) at different current densities (10, 20 and 30 mA cm^{-2}). Consistent with previous observations, Sn progressively increased as the $[Cu^{2+}]/[Sn^{2+}]$ molar ratio was decreased, with the lowest Sn content generally observed at $[Cu^{2+}]/[Sn^{2+}]$ = 10, while catalysts electrodeposited from a bath with a $[Cu^{2+}]/[Sn^{2+}]$ molar ration of 1 presented the highest Sn content. For the Cu-rich case at [Cu]/[Sn] = 10, Sn content remained low (around 4.5%), highlighting the limited incorporation of Sn under these conditions. At an intermediate $[Cu^{2+}]/[Sn^{2+}]$ molar ratio of 5, Sn content rose significantly, reaching values around 7.5%, indicating more efficient co-deposition of Sn alongside Cu. At $[Cu^{2+}]/[Sn^{2+}]$ = 1, CuSn catalysts generally had a Sn content 12%.

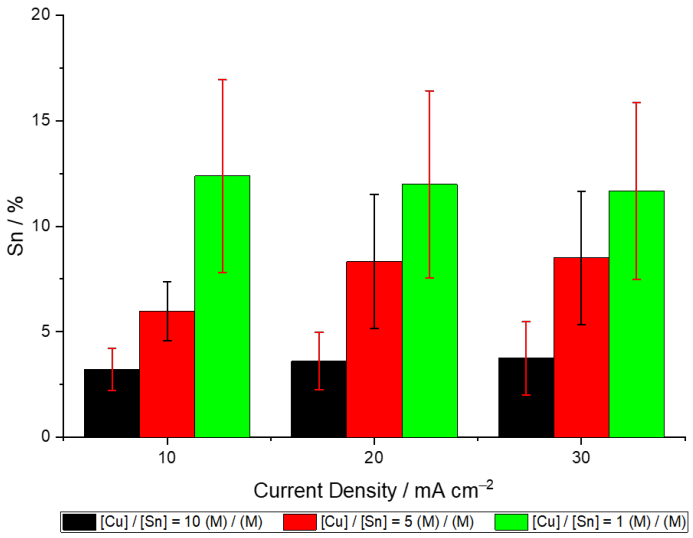


Figure 6. Sn content in CuSn electrocatalysts electrodeposited from a MSA bath with different $[Cu^{2+}]/[Sn^{2+}]$ molar ratios under various current densities. Catalyst loading = 2 C cm^{-2}. Error bars represent the standard deviation of five measurements obtained from several CuSn catalyst samples produced in said conditions.

These results demonstrate that Sn incorporation, in the electrodeposition bath used under the evaluated conditions, was primarily controlled by the $[Cu^{2+}]/[Sn^{2+}]$ molar

ratio in the electrolyte, whereas the applied current density had no significance in the composition of the CuSn catalysts (a more uniform local distribution of catalysts was still generally achieved at higher current densities, as discussed previously and reported in Figures A8–A10 and A12. This observation highlights that, under the evaluated conditions, bath chemistry rather than deposition kinetics governs the overall composition of CuSn catalysts. Importantly, the ability to reproducibly reach double-digit percentage of Sn content provides a reliable route to engineer Sn-rich catalysts, which are expected to enhance formate selectivity during CO_2 electrolysis, as proven later in the manuscript.

2.2.2. Phase Structure

The crystalline phases of the electrodeposited CuSn catalysts were investigated by XRPD for Cu/Sn molar ratios of 10, 5, and 1 at current densities of 10, 20, and 30 mA cm^{-2}. The diffractograms revealed that the XRPD data recorded in all cases matched well the crystallographic data of Cu, Sn, Cu_3Sn and graphite contained in the Crystallographic Information Framework (CIF) files COD ID 5000216, 1534488, 2310774 and 9000046, respectively, available in the Crystallography Open Database (COD) [80]. This confirmed the coexistence of metallic Cu, metallic Sn and intermetallic Cu_3Sn phases, in addition to the characteristic reflections of the carbonaceous GDL.

For catalysts prepared from the bath with a $[Cu^{2+}]/[Sn^{2+}]$ molar ratio of 10 (Figure 7), the patterns were dominated by reflections of metallic Cu at $2\theta \approx 43.3°$ (Cu(111)), 50.4° (Cu(200)), and 74.1° (Cu(220)), while weaker peaks corresponding to different Sn phases at $2\theta \approx 44.9°$ (Sn(211)) and 55.3° (Sn(301)) were also be detected. Importantly, intermetallic Cu_3Sn phases were observed at $2\theta \approx 29.5°$, 42.8°, and 62.7°, indicating partial alloying between Cu and Sn. Increasing the current density from 10 to 30 mA cm^{-2} resulted in an increase of the relative intensity of Cu_3Sn reflections, suggesting that higher deposition rates promote alloy formation. Meanwhile, the persistence of strong Cu reflections demonstrates that Cu remained the dominant crystalline component at this molar ratio.

In contrast, for catalysts prepared from the bath with a $[Cu^{2+}]/[Sn^{2+}]$ molar ratio of 5 (Figure 8), the intensity of Sn reflections became, to some extent, more pronounced, particularly at $2\theta \approx 44.9°$ (Sn(211)) and 55.3° (Sn(301)), while Cu peaks decreased in relative intensity compared to those observed in the catalysts deposited from the bath with a $[Cu^{2+}]/[Sn^{2+}]$ molar ratio of 10. Cu_3Sn reflections were again consistently observed and became sharper at higher current densities, indicating a higher proportion of the intermetallic phase. The presence of both metallic Sn and Cu_3Sn suggests incomplete alloying, with residual Sn co-deposited alongside the alloy domains.

For catalysts electrodeposited from the bath with a $[Cu^{2+}]/[Sn^{2+}]$ molar ratio of 1 (Figure 9), the XRPD patterns were dominated by Sn and Cu_3Sn phases, while Cu reflections were significantly suppressed. This indicates a transition from Sn-poor to Sn-rich microstructures as the bath stoichiometry shifts. At 30 mA cm^{-2}, the Cu_3Sn reflections, particularly at $2\theta \approx 29.5°$ and 42.8°, were intensified, consistent with enhanced intermetallic formation at higher current density. The relative suppression of metallic Cu reflections in these samples indicates that a lower $[Cu^{2+}]/[Sn^{2+}]$ molar ratio favoured the growth of Sn-rich alloys/intermetallics.

Overall, the XRPD results demonstrate that both the $[Cu^{2+}]/[Sn^{2+}]$ molar ratio ratio and the applied current density influence the crystalline phase composition. Higher current densities promote alloying, as evidenced by stronger Cu_3Sn reflections, while the $[Cu^{2+}]/[Sn^{2+}]$ molar ratio dictates whether the deposits are Sn-poor (ratio 10) or Sn-rich (ratio 1). These structural trends are expected to play a crucial role in determining the electrocatalytic properties of the CuSn catalysts, particularly in relation to their selectivity toward CO_2 reduction products.

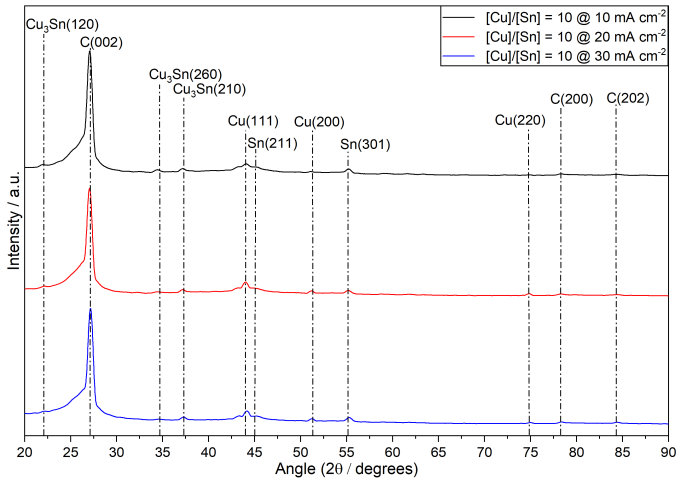


Figure 7. XRPD data collected on GDEs with 2 C cm^{-2} worth of CuSn catalysts electrodeposited on carbonaceous GDLs from a MSA bath with a $[Cu^{2+}]/[Sn^{2+}]$ molar ratio of 10 at different current densities (10, 20 and 30 mA cm^{-2}).

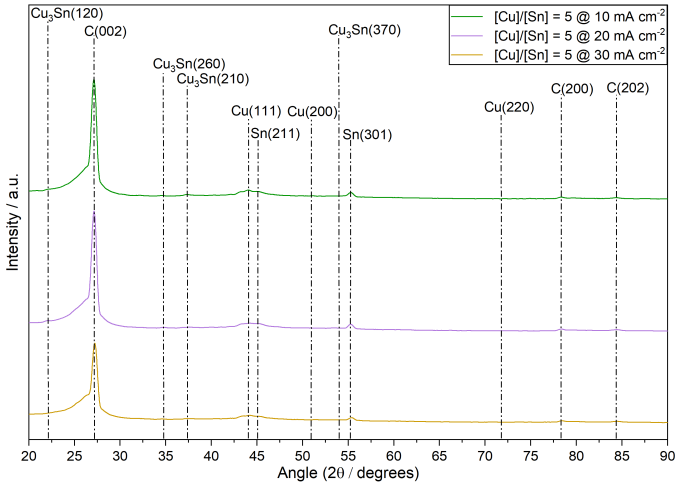


Figure 8. XRPD data collected on GDEs with 2 C cm^{-2} worth of CuSn catalysts electrodeposited on carbonaceous GDLs from a MSA bath with a $[Cu^{2+}]/[Sn^{2+}]$ molar ratio of 5 at different current densities (10, 20 and 30 mA cm^{-2}).

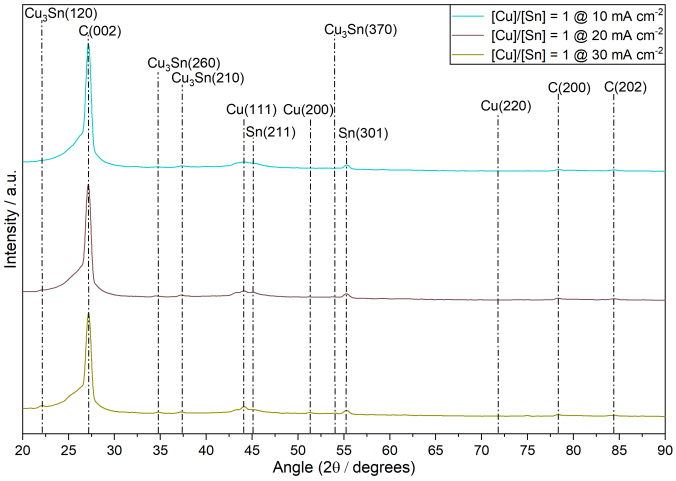


Figure 9. XRPD data collected on GDEs with 2 C cm^{-2} worth of CuSn catalysts electrodeposited on carbonaceous GDLs from a MSA bath with a $[Cu^{2+}]/[Sn^{2+}]$ molar ratio of 1 at different current densities (10, 20 and 30 mA cm^{-2}).

2.2.3. Electrochemical Characterisation

The double-layer capacitance (C_{dl}) [81,82] of GDEs containing CuSn catalysts was also obtained by recording cyclic voltammograms within a potential window of ±50 mV versus the OCP in 1 M KOH at scan rates of 20–120 mV s^{-1} with the objective to estimate the electrochemically active surface area (ECSA) of the electrodes. C_{dl} was calculated from the slope of $i_c = (i_{anodic} - i_{cathodic})/2$ versus (ν). An apparent trend was initially observed where C_{dl} decreased as the deposition current density increased from 10 to 30 mA cm^{-2} with no dependence on the $[Cu^{2+}]/[Sn^{2+}]$ molar ration (Figures A13–A15). As discussed before, higher current densities generally result in a more uniform distribution of catalysts, leading to a semi-continuous coverage of the GDL surface at a certain point [38], thereby limiting the contribution of the underlying porous carbon support to the overall capacitance. Conversely, at lower deposition currents, catalyst growth is more localised, leaving portions of the GDL exposed and resulting in higher apparent C_{dl}. However, the bare GDL (Figure A16) presented a capacitance significantly larger than the GDEs with the electrodeposited CuSn (10.204 mF cm^{-2}) due to its highly porous and rough structure, indicating that this approach may not be the most suitable to realistically compare the electrochemical surface area in the electrodes fabricated in this study, as previously discussed by the authors [38]. In any case, the resulting values for the bare GDL and the GDEs with electrodepositerd CuSn catalysts are summarised in Table 2 and Figure 10, illustring the order of magnitude difference between the capacitance of the bare substrate and that of the electrodeposited catalysts.

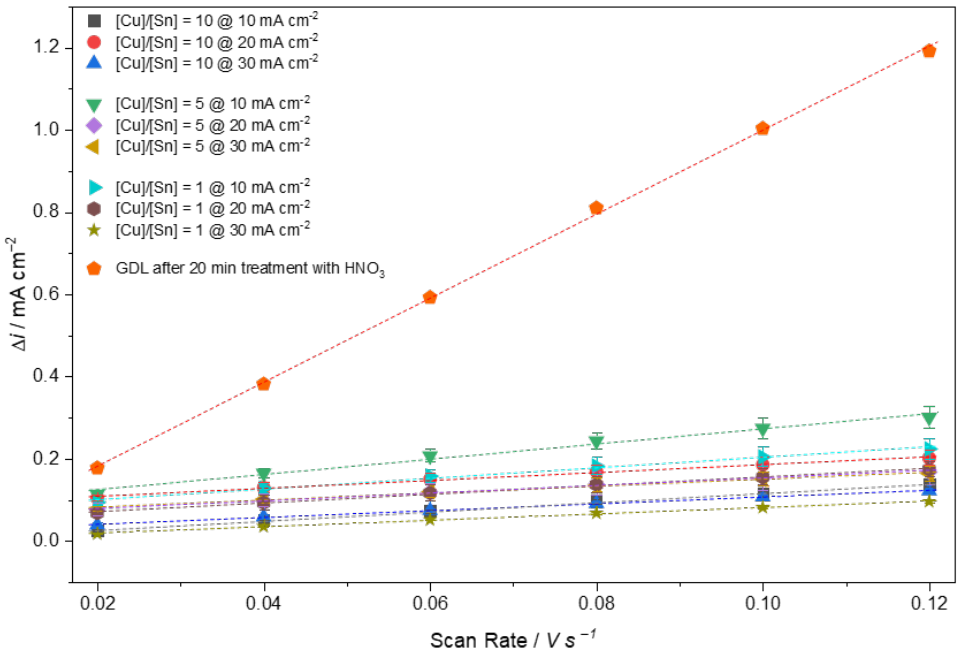


Figure 10. Double-layer charging current density difference obtained from CVs conducted over GDEs with 2 C cm^{-2} worth of CuSn catalysts electrodeposited on carbonaceous GDLs from a MSA bath with varying $[Cu^{2+}]/[Sn^{2+}]$ molar ratios (1, 5 and 10) at different current densities (10, 20 and 30 mA cm^{-2}). Data for bare GDLs is also included.

2.3. CO_2 Electrolysis Experiments

As one of the goals of this study was to evaluate the influence of the incorporation of Sn into Cu-based catalysts and the potential effect of the distribution of catalysts over the surface of the supports, four representative CuSn catalysts electrodeposited on carbonaceous GDLs with an active electrode geometrical area of 5 cm^2 were selected for CO_2 electrolysis in a flow cell configuration (Table 3) based on contrasting catalyst distribution

and Sn content, encompassing low- and high-Sn-content CuSn catalysts with both low and high C_{dl} values.

Table 2. Double-layer capacitance obtained from CVs conducted over GDEs with 2 C cm^{-2} worth of CuSn catalysts electrodeposited on carbonaceous GDLs from a MSA bath with varying $[Cu^{2+}]/[Sn^{2+}]$ molar ratios (1, 5 and 10) at different current densities (10, 20 and 30 mA cm^{-2}).

Current Density (mA cm^{-2})	$[Cu^{2+}]/[Sn^{2+}]$ = 10		$[Cu^{2+}]/[Sn^{2+}]$ = 5		$[Cu^{2+}]/[Sn^{2+}]$ = 1	
	C_{dL} (mF cm^{-2})	Error (mF cm^{-2})	C_{dL} (mF cm^{-2})	Error (mF cm^{-2})	C_{dL} (mF cm^{-2})	Error (mF cm^{-2})
10	1.121	0.014	1.848	0.024	1.288	0.017
20	0.959	0.004	0.925	0.017	1.057	0.018
30	0.826	0.004	0.845	0.014	0.777	0.003

Table 3. Electrodeposition conditions and properties of the four CuSn catalysts with an active electrode geometrical area of 5 cm^2 selected for CO_2 electrolysis.

Sample ID	$[Cu^{2+}]/[Sn^{2+}]$ Molar Ratio	Current Density (mA cm^{-2})	Sn Content (%)	C_{dL} (mF cm^{-2})
a	10	10	3.2	1.121
b	10	30	3.7	0.826
c	1	10	12.4	1.288
d	1	30	11.7	0.777

As shown in Figure 11, three of the four CuSn catalysts tested, namely "b" (catalyst containing 3.7% of Sn electrodeposited from a bath with a $[Cu^{2+}]/[Sn^{2+}]$ molar ratio of 10 at a current density of 30 mA cm^{-2}), "c" (catalyst containing 12.4% of Sn electrodeposited from a bath with a $[Cu^{2+}]/[Sn^{2+}]$ molar ratio of 1 at a current density of 10 mA cm^{-2}) and "d" (catalyst containing 11.7% of Sn electrodeposited from a bath with a $[Cu^{2+}]/[Sn^{2+}]$ molar ratio of 1 at a current density of 30 mA cm^{-2}), primarily yielded formate, CO and H_2 across the full range of current densities applied during the CO_2 electrolysis experiments, besides some traces of C_2H_4 and CH_4. The relative share of H_2 produced during the experiments generally decreased with increasing Sn content, reflecting the suppression of HER in favour of CO_2 reduction. In contrast, the catalyst with the lowest Sn contest, catalyst "a " (containing 3.2% of Sn electrodeposited from a bath with a $[Cu^{2+}]/[Sn^{2+}]$ molar ratio of 10 at a current density of 10 mA cm^{-2}), exhibited broader product selectivity, generating not only formate, CO and H_2, but also significant amounts of CH_3COO^- and higher-order C2 products (C_2H_4, C_2H_5OH), as well as traces of CH_4 and even C3 products (C_3H_7OH).

To visualise and interpret the results obtained, the partial current densities for the electrochemical reduction of CO_2 to formate and CO were plotted against the recorded corrected cathode potential (Figure 12). As we can see, even though the values of the partial current density do not account for any CO that may have been consumed as an intermediate in the production of other products [83], there was no significant difference in the performance of the catalysts tested regarding the electrochemical reduction of CO_2 to CO as all CuSn catalysts exhibited nearly identical CO partial current densities over the examined potential range. The strong overlap of both mean values and error bars observed, together with similar onset potentials and current–potential slopes, indicate that no statistically significant differences in CO_2-to-CO performance was observed among the catalysts, suggesting that CO formation was governed by a common active site rather than by catalyst-specific effects. In this case, it is very likely that the active common site was the surface of Cu grains with a [111] orientation, which are more prone to yield C1 products

like CO or CH_4 [84], based on the relatively strong peaks observed for Cu(111) planes in the XRDP analysis conducted during this study (Figures 7–9).

In contrast to CO, clear performance differences were observed for the electrochemical reduction of CO_2 to formate among the CuSn catalysts tested, as the partial current density toward $HCOO^-$ increased systematically with increasing Sn content: catalyst "a" (3.2% Sn) < catalyst "b" (3.7% Sn) < catalyst "c" (11.7% Sn) < catalyst "d" (12.4% Sn). At a given potential, the separation between the mean values clearly exceeds the associated experimental uncertainty, and distinct onset potentials and current–potential trends are observed for the different catalysts. These results indicate statistically significant differences in formate production across the catalyst series, in contrast to the behaviour observed for the electrochenmical reduction of CO_2 to CO. The observed ordering directly reflects the Sn content of the catalysts, consistent with the XRDP analysis, which identified Sn(301) grains and Cu_3Sn intermetallic phases in all samples, with increasing prominence at higher Sn loadings (Figures 7–9).

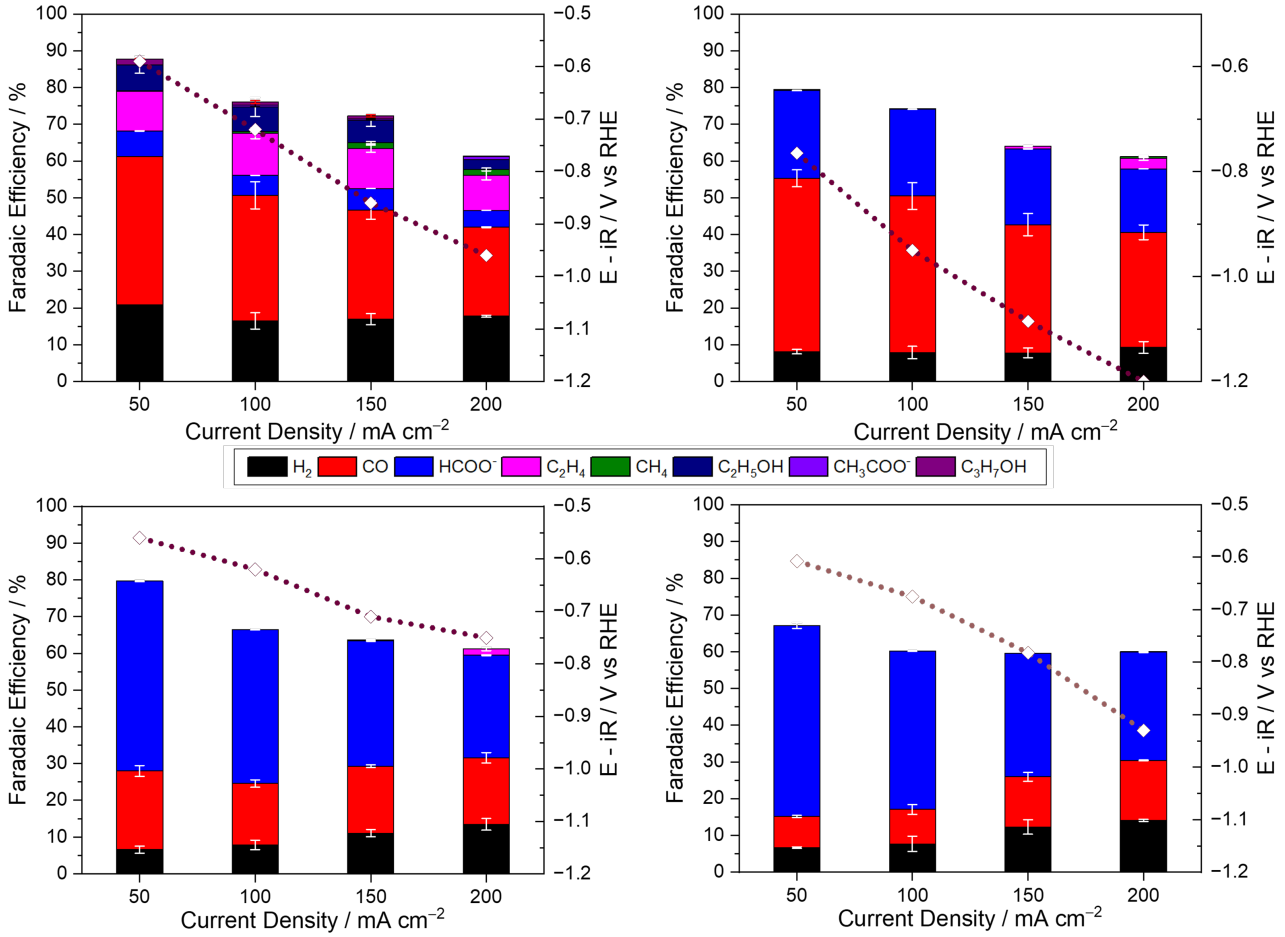


Figure 11. Faradaic efficiency values estimated for the main products obtained (left axis) and *iR*-corrected cathode potentials (right axis) recorded during CO_2 electrolysis experiments conducted at various current densities with GDEs containing 2 C cm^{-2} worth of CuSn electrocatalysts "a" (**top left**), "b" (**top right**), "c" (**bottom left**) and "d" (**bottom right**), as defined in Table 3.

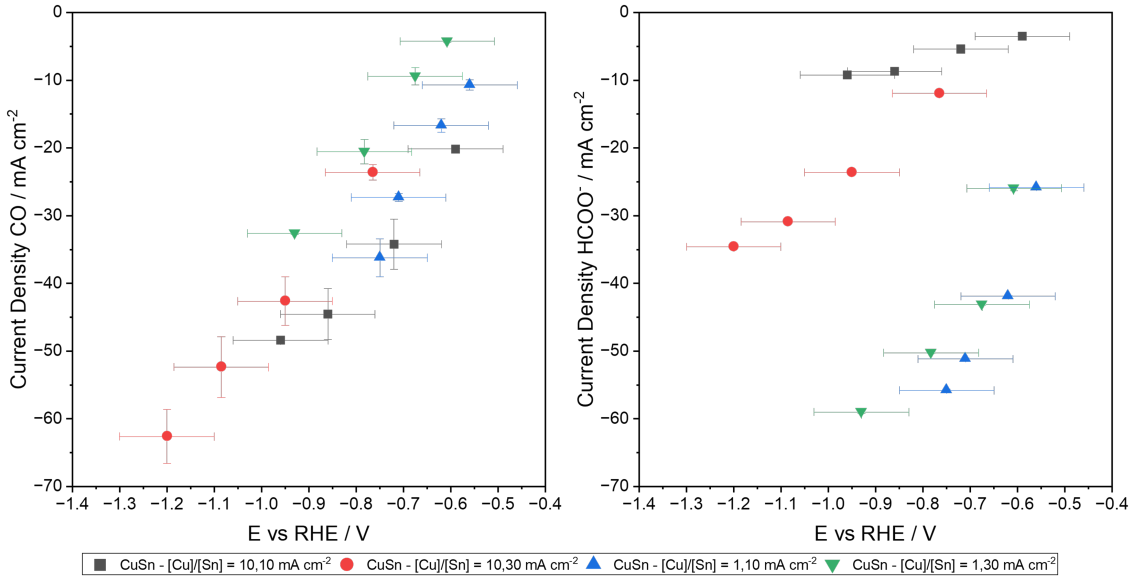


Figure 12. Partial current densities for the electrochemical reduction of CO_2 to either CO (**left**) and $HCOO^-$ (**right**) vs. *iR*-corrected cathode potentials measured during CO_2 electrolysis experiments conducted at various current densities with GDEs containing 2 C cm^{-2} worth of CuSn electrocatalysts "a" (grey swuare), "b" (red circle), "c" (blue triangle) and "d" (inversed green triangle), as defined in Table 3.

3. Discussion

The electrodeposition strategy employed in this work demonstrates that careful optimisation and control of bath composition and deposition charge is crucial for achieving reproducible CuSn coatings on commercial GDLs. The results from Tables 1 and 2 and Figures 2 and 6 highlight the strong dependence of Sn incorporation on the $[Cu^{2+}]/[Sn^{2+}]$ molar ratio in the plating bath, whereas current density primarily influences coverage and uniformity. This agrees with previous reports on electrodeposited CuSn systems, where bath chemistry rather than deposition kinetics dominated alloy composition [78]. Importantly, our results extend these findings to larger electrode areas (5 cm^2) and carbonaceous support for the preparation of GDEs for CO_2 electrolysis.

The CV study confirmed that the large potential gap between the reduction of Cu and Sn limits co-deposition to potentials below –0.40 V vs. Ag/AgCl. Under these conditions, alloy formation is achieved, but preferential Cu deposition at low charges explains why Sn-poor catalysts dominated at early plating stages, while becoming Sn-rich after a while. The addition of DAT seemed to slightly shift the Cu to more negative values and partly suppress the recorded current densities for said peak, indicating that DAT may act as a kinetic inhibitor for the electroreduction of C^{2+} to Cu. This stabilising effect may result in a more controlled nucleation while enhancing dissolution reversibility, consistent with studies on organic additives in alloy electrodeposition [72,78,79].

The catalytic evaluation in flow cells further highlighted the role of Sn incorporation and catalyst distribution in dictating CO_2RR selectivity. Three of the four catalysts selected from Table 3 primarily produced formate, CO, and H_2, with formate increasingly favoured at higher Sn contents. This trend is consistent with the composition-dependent formate activity observed in the partial current density measurements and reflects the ability of Sn-containing sites to stabilise *OCHO while suppressing HER [16]. In contrast, the fourth catalyst exhibited a broader product spectrum that included CH_4, acetate, ethanol, and trace amounts of propanol. This behaviour suggests that a balance between Cu sites, which promote *CO adsorption and C–C coupling, and Sn sites, which favour formate formation via *OCHO stabilisation, is required to access higher-order products, consistent

with reports that surface composition and site accessibility govern the transition from two-electron to multi-electron CO_2 reduction pathways. Although both CO and $HCOO^-$ are produced through two-electron, two-proton transfer processes, their formation on Cu- and Sn-containing electrocatalysts follows distinct mechanistic routes determined by the affinity of each metal for key reaction intermediates. On Cu, CO_2 reduction proceeds predominantly through the *COOH pathway, in which adsorbed CO_2 undergoes proton–electron transfer to form *COOH, followed by dehydration to yield *CO and water. The moderate binding strength of *CO on Cu enables either CO desorption or further surface coupling to C_2^+ products [16,41,60,85–88]. In contrast, Sn favours the stabilisation of oxygen-bound intermediates, particularly *OCHO, which predominantly lead to formate, while its higher *H adsorption barrier suppresses HER [89,90]. Weak *CO adsorption on Sn inhibits both CO desorption and C–C coupling, thereby suppressing multicarbon formation [15,61,62,78]. In the CuSn catalysts presented here, these mechanistic pathways would coexist, with Cu-like sites governing CO formation (and *CO-mediated coupling in some cases), while Sn-derived sites selectively enhance formate production through *OCHO stabilisation, consistent with the distinct compositions observed experimentally.

Overall, the study demonstrates that electrodeposited CuSn catalysts can be tuned by adjusting bath composition, deposition charge, and current density to target either formate-rich or syngas-type product streams. Furthermore, surface distribution and composition emerge as key descriptors for enabling multi-carbon selectivity. Future research should focus on correlating local morphology with product distribution, extending stability tests, and exploring scaling strategies for industrially relevant electrode areas.

4. Methodology

4.1. Chemicals and Materials

All chemical reagents used in this study were of technical or analytical grade and used as received, without any additional purification steps. Copper(II) sulfate pentahydrate ($CuSO_4 \cdot 5\,H_2O$, 99 + %), tin (II) sulfate ($SnSO_4$, 95%) and 3,5-diamino-1,2,4-triazole (DAT, 98%) from Thermo Fisher Scientific (Waltham, MA, USA) were dissolved in deionised water to prepare electrolyte baths at room temperature (25 °C); methane sulfonic acid (CH_4O_3S, 70%), also from Thermo Fisher Scientific, was added to the electroplating until the required concentration was achieved. Carbonaceous Sigracet 36 BB gas diffusion layers (GDLs), manufactured by SGL Carbon and supplied by Fuel Cell Store, were used as substrates for the CuSn catalysts in order to fabricate the gas diffusion electrodes (GDEs) evaluated in this study. 70% nitric acid (HNO_3) from Sigma-Aldrich (St. Louis, MO, USA) was used for the pretreatment of the carbon-based GDLs. Potassium hydroxide (KOH, >85%) from Sigma-Aldrich was used for ECSA analysis.

4.2. GDE Preparation

As pointed above, carbonaceous GDLs were used as substrates for the fabrication of GDEs via electrodeposition of CuSn electrocatalysts. Electroplating baths for the in-situ synthesis of the catalysts were prepared with varying Cu:Sn molar ratios by combining two copper concentrations (0.05 M and 0.1 M) and three Sn concentrations (0.01 M, 0.025 M, and 0.05 M), along with 10 mM of 3,5-diamino-1,2,4-triazole (DAT) as an additive, all in an aqueous solution containing 2.4 M methane sulfonic acid (MSA). The electrodeposition of the catalysts on the carbon-based GDLs was carried out under galvanostatic conditions at varying current densities ranging from 8 to 30 mA cm^{-2}. Catalyst loading was controlled by the total charge transferred during deposition, and all experiments were conducted at a constant bath temperature of 35 °C.

The objective of the synthesis research was to optimise the distribution of Cu and Sn across the GDL surface and enhance the reproducibility of electrode manufacturing. Table 4 summarises the electroplating parameters, with optimisation efforts centered on a charge density (Q) of 2 C cm^{-2} and current densities of 10, 20, and 30 mA cm^{-2} for further study.

Table 4. Electroplating Bath compositions used for CuSn catalyst synthesis.

Parameter	Values		
Cu/M	0.200	0.1	0.05
Sn/M	0.025, 0.01, 0.005	0.05, 0.025, 0.01	0.05, 0.025, 0.01
Molar Ratio [Cu]/[Sn]	8, 20, 40	2, 4, 10	1, 2, 5
Charge Density/C cm^{-2}	2	1, 2, 4	1, 2, 4
Current Density/mA cm^{-2}	8, 10, 15, 20, 30	8, 10, 15, 20, 30	8, 10, 15, 20, 30

In electrochemical processes requiring a large specific surface area to facilitate gas diffusion, the selection of a suitable substrate for constructing a GDE is essential. A GDE must permit efficient gas and product transport while preventing flooding of the gas compartment by aqueous electrolytes. Carbon paper is a widely used porous substrate due to its chemical stability, low cost, and commercial availability [91–93]. Ideally, carbon paper should be hydrophilic on one side to enable metal deposition and hydrophobic on the other to prevent flooding. However, the use of PTFE in the preparation of the microporous layer in carbon-based GDLs (i.e., the area where catalysts are applied) makes that side of the GDL highly hydrophobic, requiring surface activation. Nitric acid (HNO_3) treatment is commonly used to introduce functional groups that improve catalyst adhesion, but full immersion can over-activate the GDL, making both sides hydrophilic and prone to flooding. To avoid this, the same approach previously developed by the authors [38] was followed in this study, which consisted in letting the GDLs float on their 'active' side (i.e., the area where the microporous layer is in contact with the electrolyte during CO_2RR) in concentrated HNO_3 for up to 1 h. This selectively activated only the side of the GDL where the electrodeposition of catalysts would occur, ensuring catalyst deposition while maintaining gas permeability and preventing flooding during CO_2 electrolysis experiments.

Following HNO_3 pre-treatment, the gas diffusion layers (GDLs) were thoroughly rinsed with deionised water to remove residual acid and prevent cross-contamination. The cleaned GDLs were then placed into a custom-engineered jig made of polyethylene terephthalate glycol (PETG) (Figure A1, Appendix A) designed to streamline the plating process and ensure accurate, uniform and reproducible deposition of the catalyst onto a defined surface area. The electrodeposition process was conducted using two versions of this custom jig: one configured for initial synthesis optimisation with a square plating area of 2.25 cm^2, and another with a 5 cm^2 area tailored for CO_2RR testing. In both electroplating setups, the PETG jig functioned as the cathode holder, while a copper foil was employed as the anode (Figure A2, Appendix A). Both electrodes were submerged in the electroplating bath and connected to an Autolab PGSTAT204 potentiostat/galvanostat (Metrohm Autolab, Utrecht, The Netherlands). A magnetic stirrer with a heated plate and thermostat (MS-H280-Pro, SciQuip, Rotherham, UK) provided optional agitation and ensured stable bath temperature throughout the process.

4.3. GDE Characterisation

Since the initial synthesis optimisation was conducted on GDEs with a square area of 2.25 cm^2, material characterisation supporting catalyst development to identify the most promising catalyst formulation for CO_2RR was only performed on these samples. Nevertheless, periodic quality checks were conducted during the fabrication of larger 5 cm^2

GDEs used in CO_2 electrolysis experiments to ensure reproducibility and consistency, as diwscussed in prior work by the authorts [38]. Surface morphology and structure of the prepared GDEs were analysed using a Quanta 600 FEG scanning electron microscope (SEM) from FEI (Hillsboro, OR, USA), which was equipped with secondary electron (SE) and backscattered electron (BSE) detectors, and was operated in low vacuum mode. On-site spectroscopic measurements were performed using energy-dispersive spectroscopy (EDS) to obtain elemental mapping and semi-quantitative compositional analysis of the catalyst surfaces. X-ray powder diffraction (XRPD) analysis was performed in prepared GDEs using a Bruker D8 Advance diffractometer (Billerica, MA, USA) with Cu Kα radiation (Bragg–Brentano geometry); data were collected over the 2θ range 35°–95° with a step size of 0.017° at a scan speed of 0.6 s per step.

To evaluate the electrochemical capacitance of the fabricated GDEs, double-layer capacitance (C_{DL}) was measured via cyclic voltammetry (CV) [81] in a potential range around the open circuit potential (OCP) where no Faradaic reactions were occurring [82]. CVs were conducted at six scan rates (20, 40, 60, 80, 100 and 120 mV s^{-1}) within a potential window of ±50 mV versus the OCP, where no Faradaic currents were observed, in a 1 M KOH aqueous solution using a standard three-electrode configuration. Custom jigs made of acrylonitrile butadiene styrene (ABS) were designed to hold the GDEs in place (Figure A3, Appendix A), with a platinum wire acting as the counter electrode and an Ag/AgCl electrode as reference (CH Instruments, Austin, TX, USA; supplied by IJ Cambria, Llwynhendy, Wales, UK). The difference between the anodic and cathodic charging currents at 0 V vs. OCP were plotted against the scan rate (ν), where the slope of the linear fit corresponded to the C_{DL}:

$$C_{DL} = \frac{\Delta i}{\nu} \quad (1)$$

4.4. Electrochemical Reduction of CO_2

Selected GDEs consisting of CuSn catalysts electrodeposited over carbon-based GDLs prepared and characterised following the methods described above were used for the electrochemical reduction of CO_2 in a customised three-compartment filter-press flow cell (Micro Flow Cell, Electrocell A/S, Tarm, Denmark), which had already been validated in previous studies by the authors [38,41].

The cell consisted of separate gas, catholyte and anolyte chambers; the GDEs evaluated in this study formed the interface between the gas and catholyte compartments, while a Fumasep FAB-PK-130 anion exchange membrane (Fumatech, Bietigheim-Bissingen, Germany; supplied by Fuel Cell Store, Bryan, TX, USA) separated the catholyte from the anolyte. The GDEs (3 cm × 3.5 cm) therefore acted as the cathode in the cell, where the deposition of the catalyst had been restricted to a central region of approximately 5 cm^2 (2 cm × 2.5 cm), whereas a commercial dimensionally stable anode (DSA) was used in the anolyte compartment as the anode in all electrolysis experiments. To ensure accurate and stable potential measurements, a leak-free Ag/AgCl reference electrode (Innovative Instruments, Tampa, FL, USA) was placed in the catholyte compartment close to the surface of the GDE being evaluated. Sealing throughout the assembly was achieved using ethylene propylene diene monomer (EPDM) gaskets to avoid gas or liquid cross-leakage.

Galvanostatic CO_2RR experiments were performed at 50, 100, 150, and 200 mA cm^{-2}. With this purpose, an external bench power supply was used to apply a constant current during the tests while the electrochemical system was connected to a Bio-Logic SP-50 potentiostat (Seyssinet-Pariset, France) operating in open-circuit mode to monitor the cathode potential. Both catholyte and anolyte chambers were filled with 1 M KOH aqueous

solution. The recorded cathodic potentials were converted to the reversible hydrogen electrode (RHE) scale using the following relation:

$$E_{\mathrm{RHE}} = E_{\mathrm{Ag/AgCl}} + 0.209 + 0.059 \cdot \mathrm{pH} \quad (2)$$

Prior to each electrolysis experiment, the CO_2 gas stream (12 mL min^{-1}) was introduced to the gas compartment and allowed to stabilise.

Gaseous reaction products were monitored using a Shimadzu GC-2030 gas chromatograph (Nakagyo-ku, Kyoto, Japan) fitted with a Carboxen®-1010 PLOT column and a barrier discharge ionisation detector (BID). For this purpose, the gas outlet of the flow cell was directly connected to the GC system, allowing for measurements to be taken automatically after the gas flow reached steady state. The Faradaic efficiency (FE) for each gaseous product i was determined based on Faraday's laws under galvanostatic conditions:

$$\mathrm{FE}_{i,\mathrm{gas}}(\%) = 100 \times \frac{n_i\, v\, M_i\, F}{J_{\mathrm{total}}} \quad (3)$$

where n_i is the number of electrons transferred per mole of product, v is the volumetric gas flow rate, M_i is the mole fraction of the product as measured by GC, F is the Faraday constant, and J_{total} is the total current applied. The gas flow was normalised to ambient conditions.

Liquid products, including alcohols and carboxylates, were identified and quantified using either headspace gas chromatography (HS-GC) or ion chromatography (IC), depending on their chemical nature. In all cases, catholyte samples were collected every 60 min and stored at 4 °C until HS-GC or IC analysis was conducted. HS-GC measurements were performed using a Shimadzu GC-2010 system equipped with an HP-PLOT Q column, where 100 µL of catholyte was transferred into 10 mL sealed autosampler vials; quantification was then performed using external calibration curves. For anionic species such as formate and acetate, a Dionex ICS-1100 system (Sunnyvale, CA, USA) with a Dionex IonPac AS-22 anion exchange column and a 4 mm ASR-ultra chemical suppressor was used for the IC analysis, where 0.5 mL samples were diluted tenfold with deionised water prior to injection; in all cases, the eluent was a mixture of 4.5 mM Na_2CO_3 and 1.4 mM $NaHCO_3$ flowing at 1.5 mL min^{-1}. The Faradaic efficiency of each liquid product i was again calculated using Faraday's Laws of Electrolysis:

$$\mathrm{FE}_{i,\mathrm{liquid}}(\%) = 100 \times \frac{n_i\, V\, M_i\, F}{Q_{\mathrm{total}}} \quad (4)$$

where n_i is the number of electrons required per mole of product i, V is the catholyte volume, M_i is the molar concentration of the product, and Q_{total} is the total charge passed during the sampling interval.

5. Conclusions

This work demonstrates a reproducible electrodeposition route for CuSn catalysts on commercial GDLs, enabling systematic tuning of composition and morphology for CO_2 electroreduction. Sn incorporation was shown to be governed by the $[Cu^{2+}]/[Sn^{2+}]$ molar ratio in the plating bath, while current density primarily controlled film coverage and uniformity. The optimal deposition condition of 2 C cm^{-2} in 1.53 M MSA produced uniform and adherent catalysts across a wide range of ratios. Electrochemical studies revealed that alloy co-deposition occurs only at sufficiently negative potentials (below –0.40 V vs. Ag/AgCl), with DAT acting as a Cu kinetic inhibitor that broadens cathodic peaks and stabilises dissolution behaviour.

Catalytic evaluation in a flow cell demonstrated that Sn-poor catalysts favoured CO and H_2, whereas Sn-rich catalysts promoted formate selectivity with Faradaic efficiencies of up to 52% at 50 mA cm^{-2}. At higher current densities (200 mA cm^{-2}), formate efficiencies of 30% were obtained, with CO and H_2 as co-products, supporting potential application in syngas production. Notably, one catalyst with specific Cu-Sn distribution generated a wider product spectrum including C1-C3 products, highlighting the importance of surface heterogeneity and synergistic effects.

In summary, electrodeposited CuSn catalysts provide a low-cost and scalable platform for CO_2RR with a tunable selectivity towards either formate or broader product mixtures by controlling Sn content and catalyst distribution. These insights advance the rational design of electrodeposited bimetallics for sustainable CO_2 conversion, while pointing to future opportunities in stability testing, surface engineering, and scale-up for practical deployment.

Author Contributions: Conceptualization, L.G.N.-T. and I.T.; methodology, L.G.N.-T., M.S.T.-O., S.M.-L. and I.T.; validation, L.G.N.-T. and M.S.T.-O.; formal analysis, L.G.N.-T. and I.T.; investigation, L.G.N.-T., S.M.-L. and I.T.; resources, L.G.N.-T., S.M.-L. and I.T.; data curation, L.G.N.-T. and I.T.; writing—original draft preparation, L.G.N.-T.; writing—review and editing, M.S.T.-O., S.M.-L. and I.T.; visualization, L.G.N.-T. and I.T.; supervision, I.T.; project administration, S.M.-L. and I.T.; funding acquisition, L.G.N.-T., S.M.-L. and I.T. All authors have read and agreed to the published version of the manuscript.

Funding: L.G.N.-T., M.S.T.-O., S.M.-L. and I.T. are grateful to the European Commission and UK Research and Innovation (UKRI) for their financial support of the SolDAC project funded through Horizon Europe (grant agreement 101069359) and Innovation Service Funding 10039331, respectively. I.T. acknowledges the support of the Carnegie Trust for the Universities of Scotland through their Research Incentive Grant RIG009799. L.G.N.-T., M.S.T.-O. and I.T. thank Consejo Nacional de Humanidades, Ciencias y Tecnologías (CONAHCYT) in Mexico for its support through two overseas PhD scholarships.

Data Availability Statement: The original contributions presented in this study are included in the article/Appendix A. Further inquiries can be directed to the corresponding authors.

Acknowledgments: During the preparation of this manuscript, the authors used OpenAI's ChatGPT-5.2 for the purposes of improving the readability, conciseness and style of some sections of the manuscript. The authors have reviewed and edited the output and take full responsibility for the content of this publication.

Conflicts of Interest: The authors declare no conflicts of interest. The funders had no role in the design of the study; in the collection, analyses, or interpretation of data; in the writing of the manuscript; or in the decision to publish the results.

Appendix A

Appendix A.1. Experimental

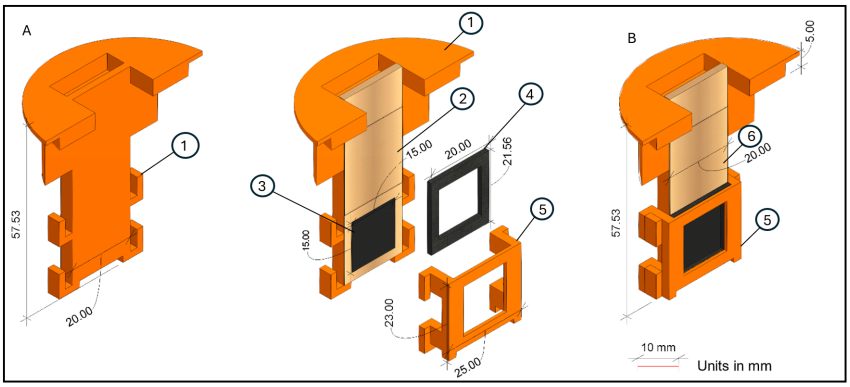


Figure A1. Schematic of the custom cathode assembly used for catalyst electrodeposition on commercial carbon-based GDLs (not to scale). (**A**) Individual Jig Components: 1. Electrode support securing the GDL during deposition, 2. Copper foil tape serving as the current collector; 3. Commercial carbonaceous GDL as the substrate for CuSn deposition; 4. EPDM gasket ensuring a tight seal and restricting deposition to the exposed GDL area in contact with the electrolyte; 5. Holder frame securing the GDL and gasket in place; 6. Kapton tape masking the foil to prevent electrolyte contact. (**B**) Complete electrode (cathode) jig assembly.

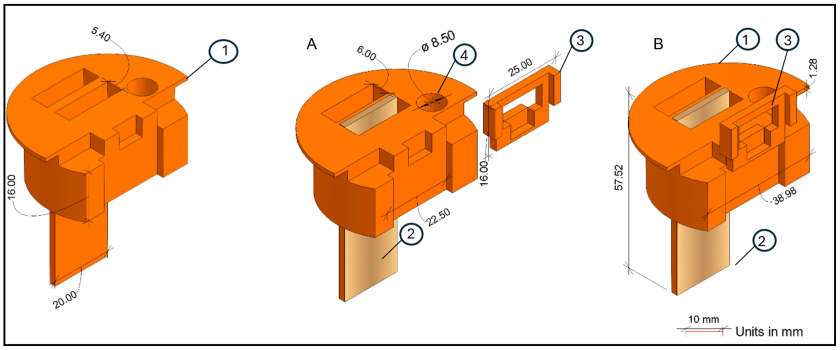


Figure A2. Schematic representation of the custom anode assembly designed for catalyst electrodeposition on commercial carbon-based GDLs (not to scale). (**A**) Individual Jig Components: 1. Electrode support; 2. Copper foil tape (anode); 3. Cap frame to seal the gap between jigs and reduce gas leakage; 4. Temperature port for sensor insertion. (**B**) Fully assembled configuration.

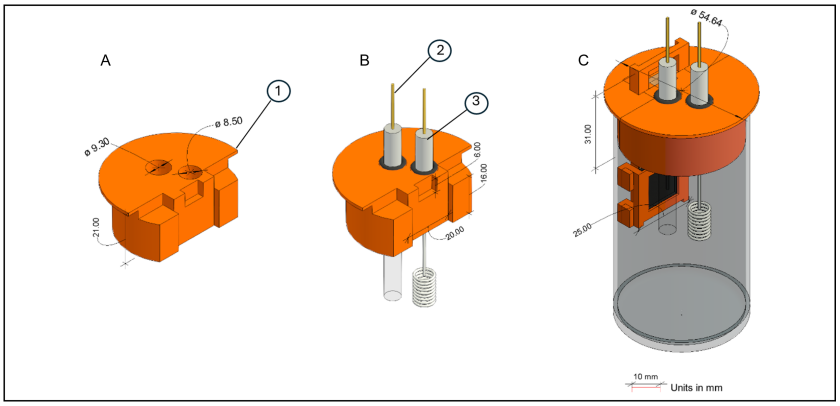


Figure A3. Schematic representation of the assembly designed for electrochemical analysis of GDEs (not to scale). (**A**) Individual Jig Components: 1. Counter GDE support to place the sensors; 2. Reference Electrode; 3. Counter (Pt) Electrode. (**B**) Assembled configuration. (**C**) Set-up configuration.

Appendix A.2. Results

Appendix A.2.1. Systematic Optimisation of Electrodeposition Conditions

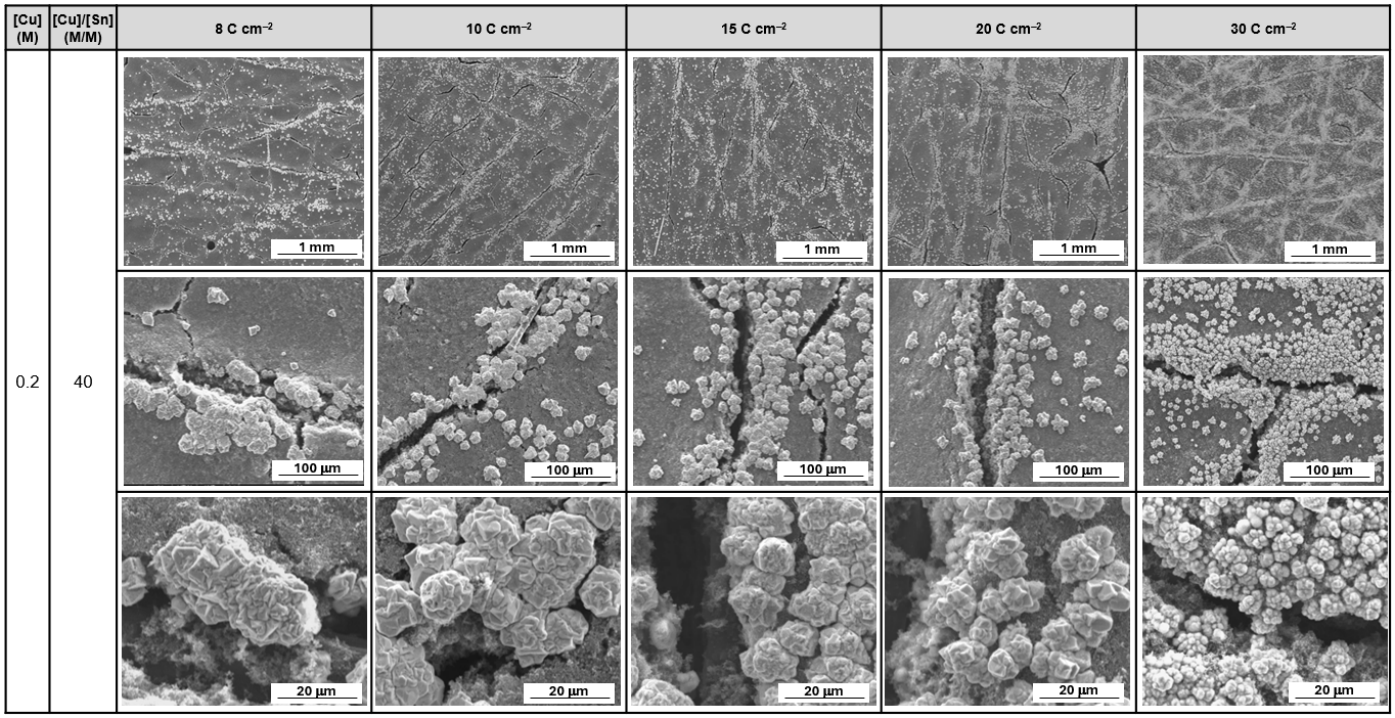


Figure A4. SEM micrographs of GDEs after electrodeposition of 2 C cm^{-2} worth of CuSn catalysts under various current densities (8, 10, 15, 20 and 30 mA cm^{-2}) on carbon-based GDLs from a 1.22 M MSA electrolyte with a $[Cu^{2+}]/[Sn^{2+}]$ molar ratio of 40 and Cu^{2+} concentration of 0.2 M.

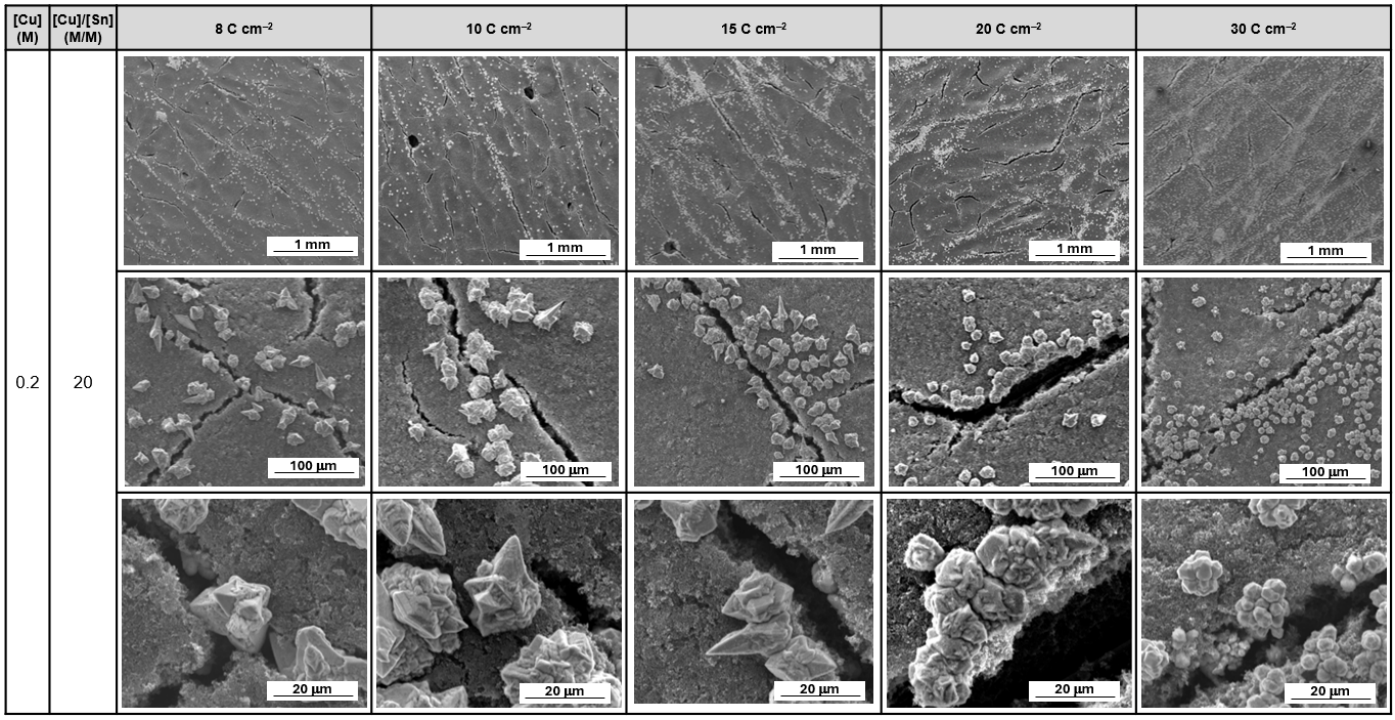


Figure A5. SEM micrographs of GDEs after electrodeposition of 2 C cm^{-2} worth of CuSn catalysts under various current densities (8, 10, 15, 20 and 30 mA cm^{-2}) on carbon-based GDLs from a 1.22 M MSA electrolyte with a $[Cu^{2+}]/[Sn^{2+}]$ molar ratio of 20 and Cu^{2+} concentration of 0.2 M.

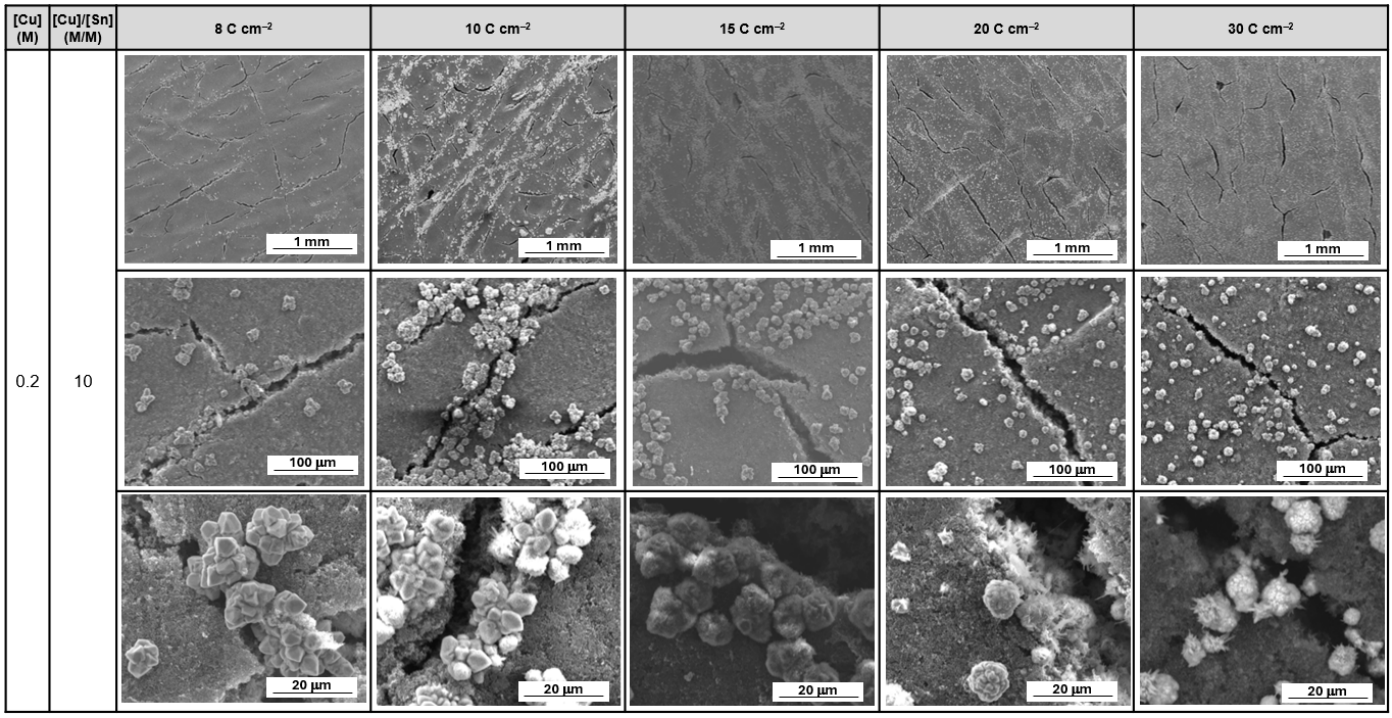


Figure A6. SEM micrographs of GDEs after electrodeposition of 2 C cm^{-2} worth of CuSn catalysts under various current densities (8, 10, 15, 20 and 30 mA cm^{-2}) on carbon-based GDLs from a 1.22 M MSA electrolyte with a $[Cu^{2+}]/[Sn^{2+}]$ molar ratio of 10 and Cu^{2+} concentration of 0.2 M.

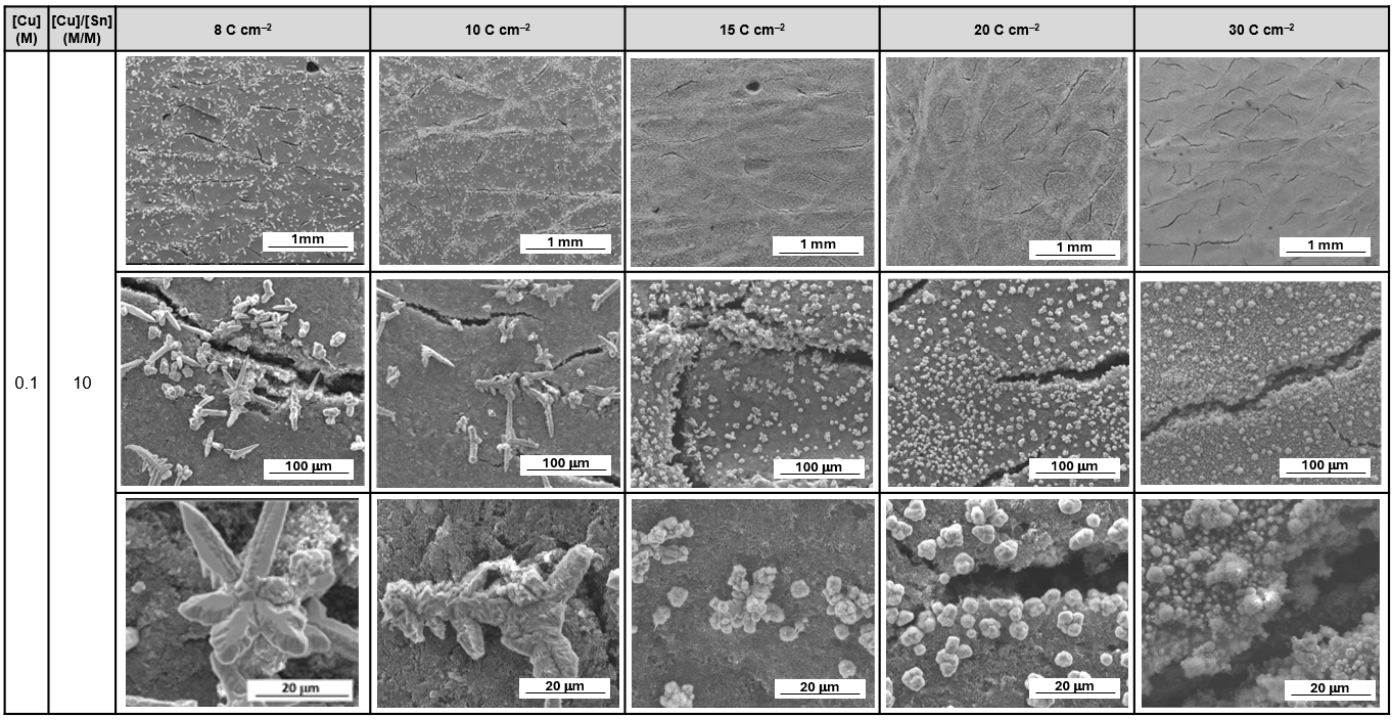


Figure A7. SEM micrographs of GDEs after electrodeposition of 2 C cm^{-2} worth of CuSn catalysts under various current densities (8, 10, 15, 20 and 30 mA cm^{-2}) on carbon-based GDLs from a 1.22 M MSA electrolyte with a $[Cu^{2+}]/[Sn^{2+}]$ molar ratio of 10 and Cu^{2+} concentration of 0.1 M.

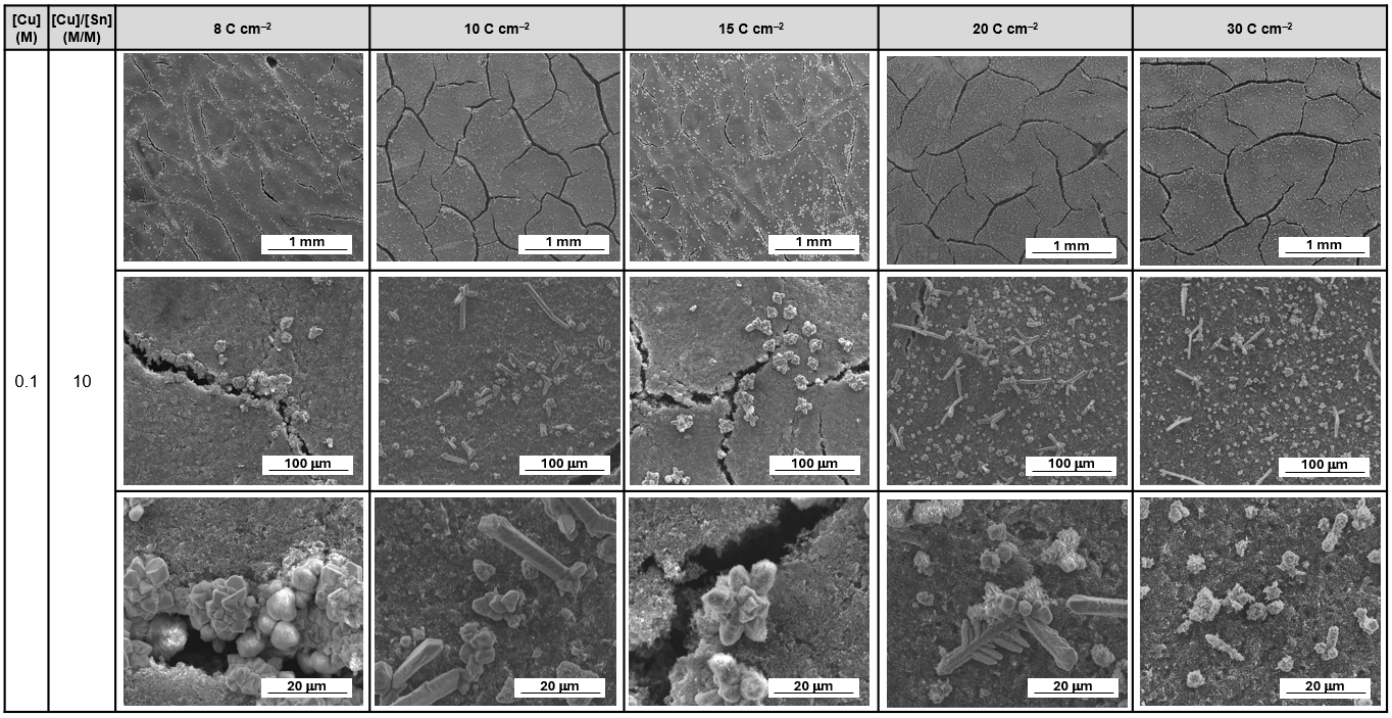


Figure A8. SEM micrographs of GDEs after electrodeposition of 2 C cm^{-2} worth of CuSn catalysts under various current densities (8, 10, 15, 20 and 30 mA cm^{-2}) on carbon-based GDLs from a 1.53 M MSA electrolyte with a $[Cu^{2+}]/[Sn^{2+}]$ molar ratio of 10 and Cu^{2+} concentration of 0.1 M.

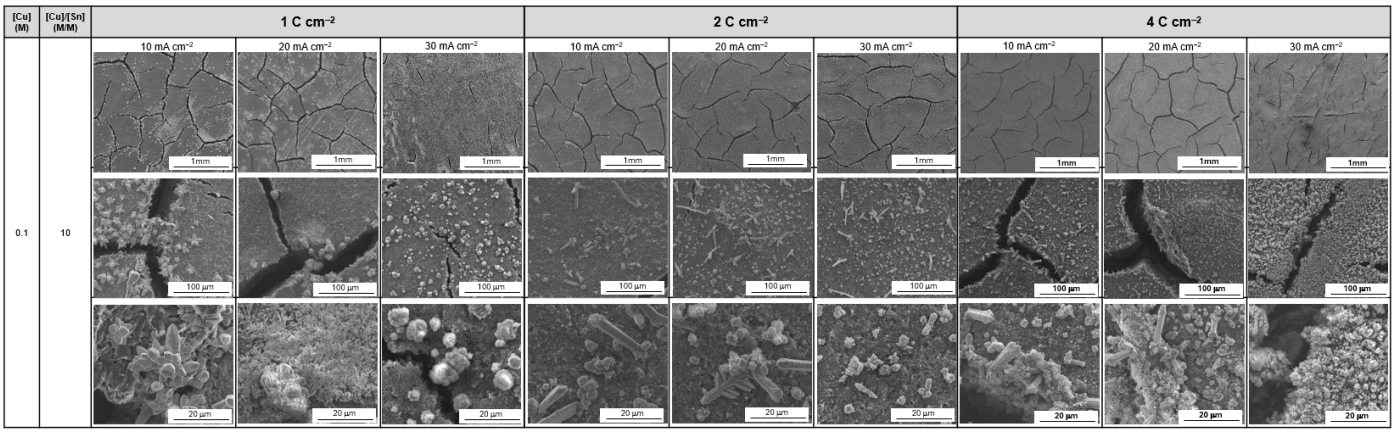


Figure A9. SEM micrographs of GDEs after electrodeposition of CuSn catalysts with different loadings (1, 2 and 4 C cm^{-2}) under various current densities (10, 20 and 30 mA cm^{-2}) on carbon-based GDLs from a 1.53 M MSA electrolyte with a $[Cu^{2+}]/[Sn^{2+}]$ molar ratio of 10 and Cu^{2+} concentration of 0.1 M.

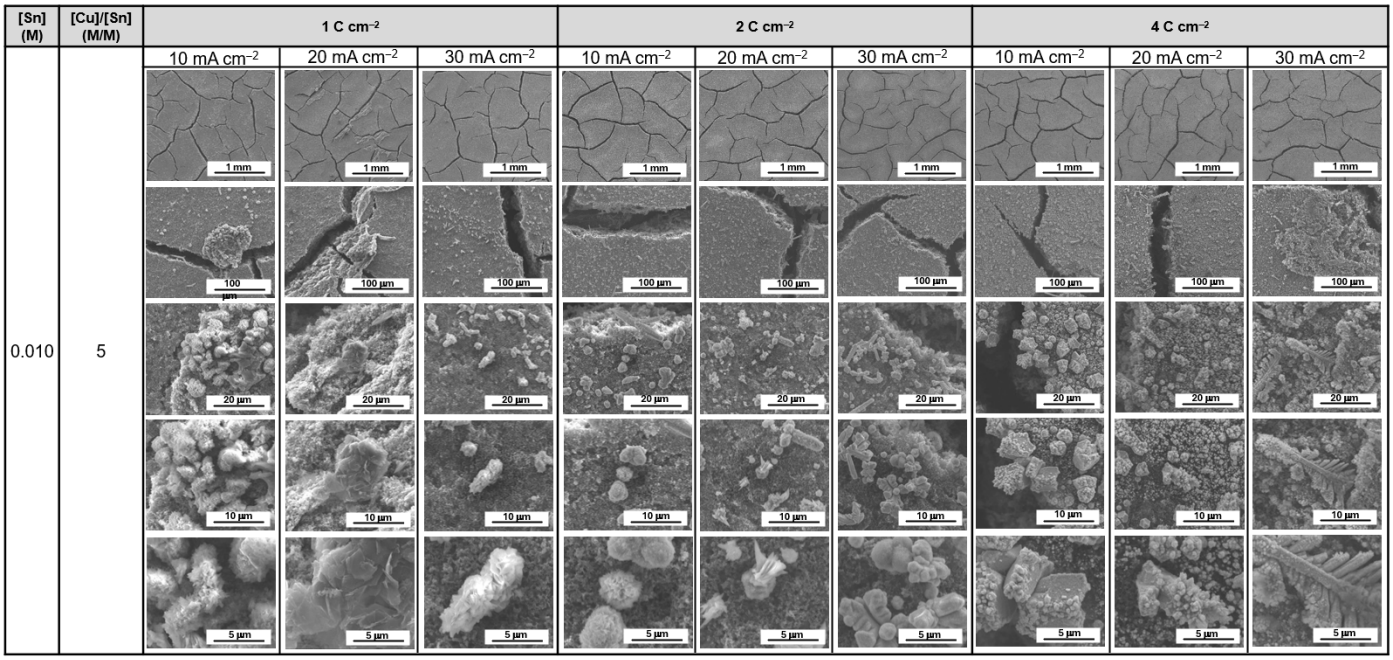


Figure A10. SEM micrographs of GDEs after electrodeposition of CuSn catalysts with different loadings (1, 2 and 4 C cm^{-2}) under various current densities (10, 20 and 30 mA cm^{-2}) on carbon-based GDLs from a 1.53 M MSA electrolyte with a $[Cu^{2+}]/[Sn^{2+}]$ molar ratio of 5 and Cu^{2+} concentration of 0.05 M.

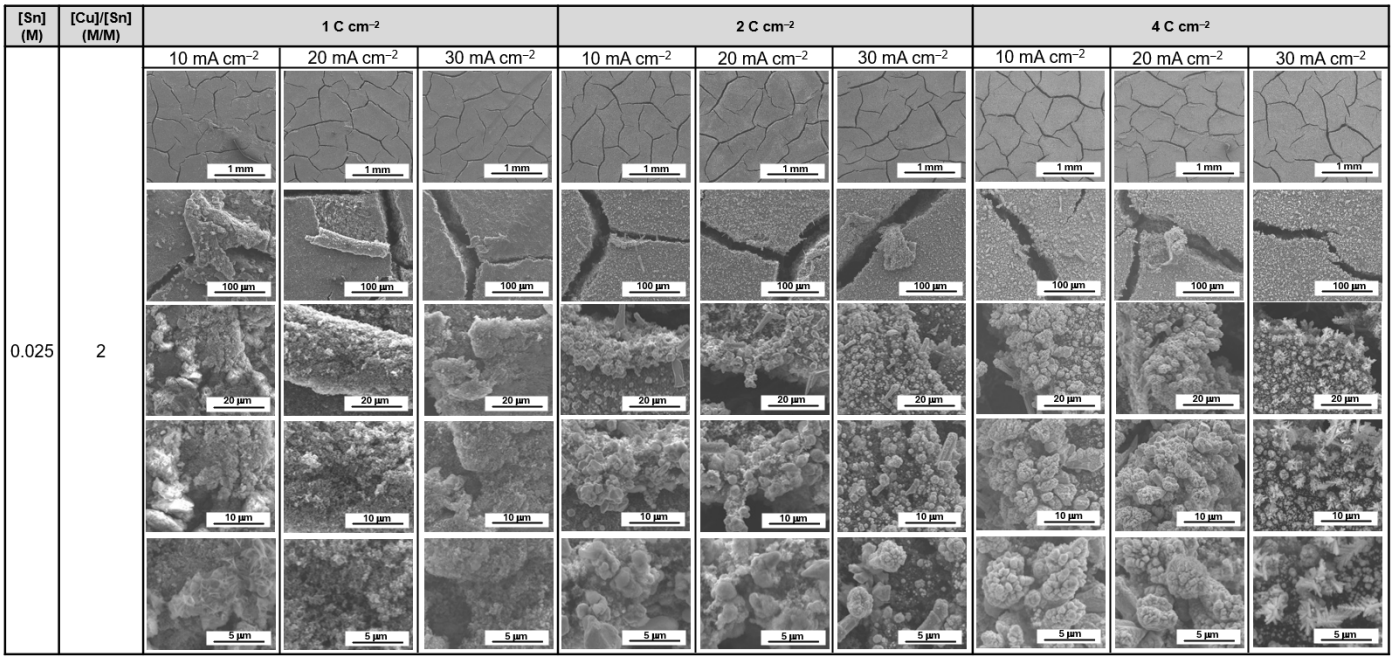


Figure A11. SEM micrographs of GDEs after electrodeposition of CuSn catalysts with different loadings (1, 2 and 4 C cm^{-2}) under various current densities (10, 20 and 30 mA cm^{-2}) on carbon-based GDLs from a 1.53 M MSA electrolyte with a $[Cu^{2+}]/[Sn^{2+}]$ molar ratio of 2 and Cu^{2+} concentration of 0.05 M.

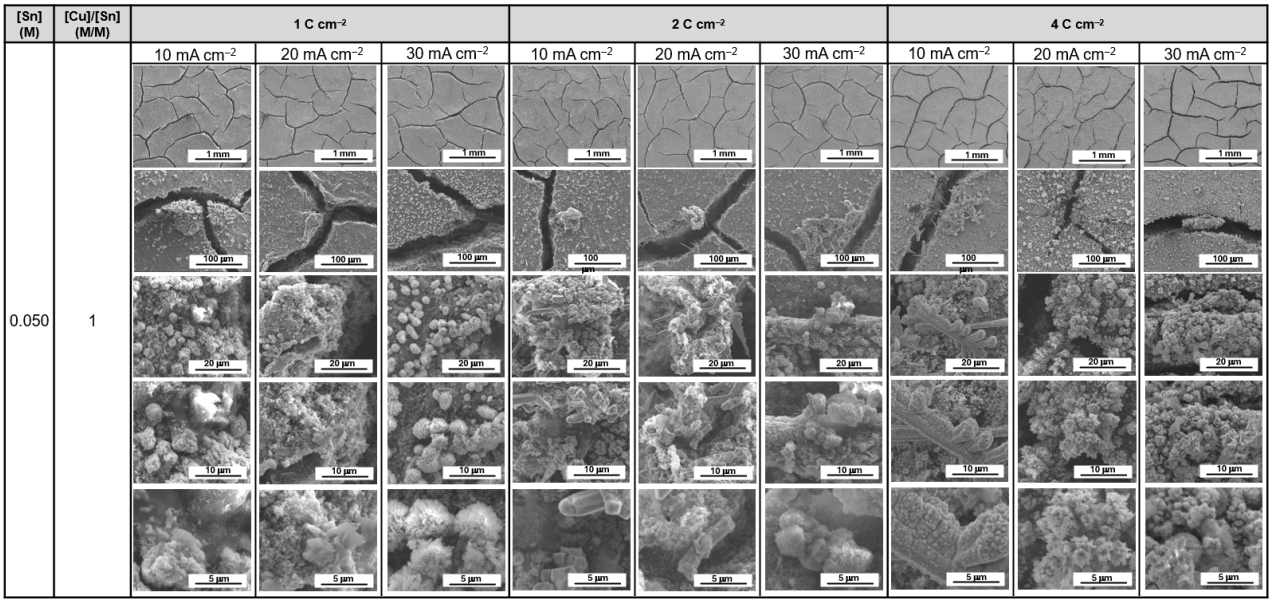


Figure A12. SEM micrographs of GDEs after electrodeposition of CuSn catalysts with different loadings (1, 2 and 4 C cm^{-2}) under various current densities (10, 20 and 30 mA cm^{-2}) on carbon-based GDLs from a 1.53 M MSA electrolyte with a $[Cu^{2+}]/[Sn^{2+}]$ molar ratio of 1 and Cu^{2+} concentration of 0.05 M.

Appendix A.2.2. Electrocatalyst Characterisation

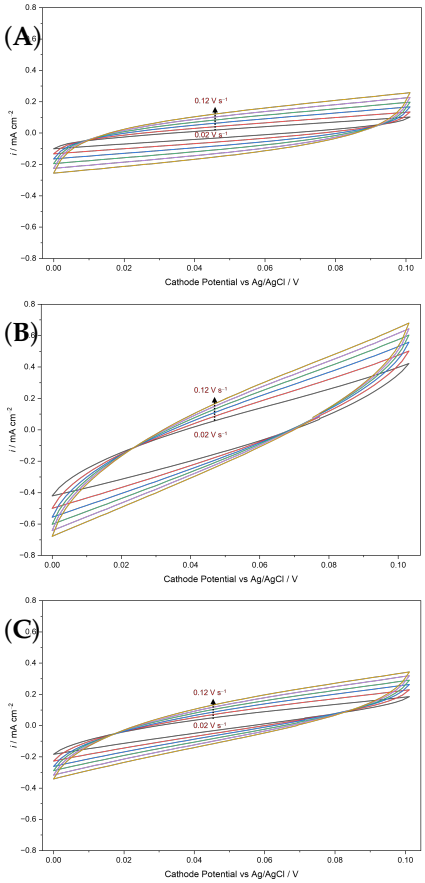


Figure A13. CVs conducted within a potential window of ±50 mV versus the OCP in 1 M KOH at scan rates of 20–120 mV s^{-1} over GDEs equipped with 2 C $cm^{-}2$ worth of CuSn catalysts electrodeposited on carbon-based GDLs from a 1.53 M MSA electrolyte with a $[Cu^{2+}]/[Sn^{2+}]$ molar ratio of 10 at different current densities: (**A**) 10 mA cm^{-2}, (**B**) 20 mA cm^{-2}, (**C**) 30 mA cm^{-2}.

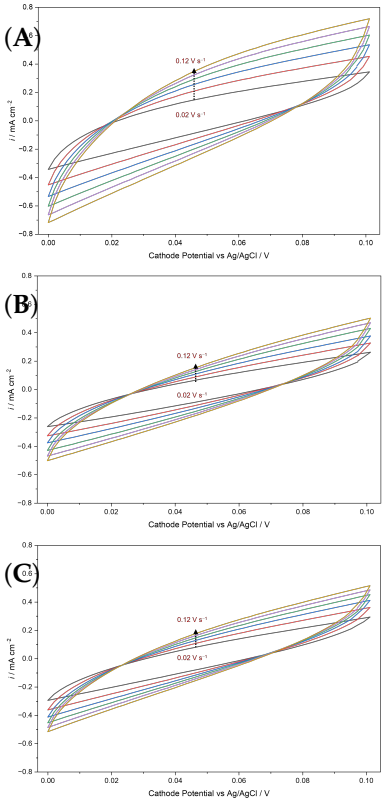


Figure A14. CVs conducted within a potential window of ±50 mV versus the OCP in 1 M KOH at scan rates of 20–120 mV s^{-1} over GDEs equipped with 2 C $cm^{-}2$ worth of CuSn catalysts electrodeposited on carbon-based GDLs from a 1.53 M MSA electrolyte with a $[Cu^{2+}]/[Sn^{2+}]$ molar ratio of 5 at different current densities: (**A**) 10 mA cm^{-2}, (**B**) 20 mA cm^{-2}, (**C**) 30 mA cm^{-2}.

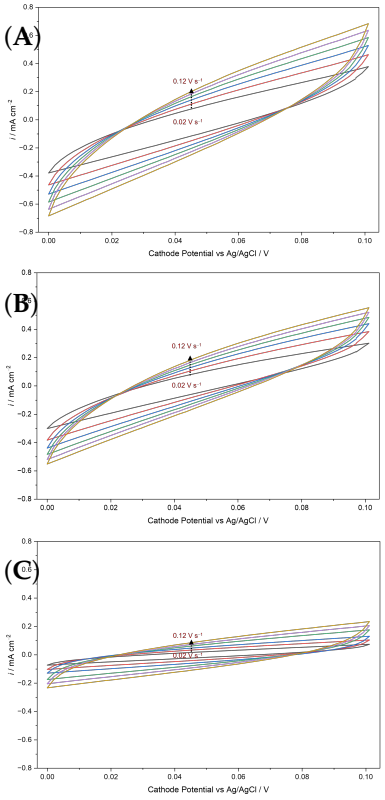


Figure A15. CVs conducted within a potential window of ±50 mV versus the OCP in 1 M KOH at scan rates of 20–120 mV s^{-1} over GDEs equipped with 2 C $cm^{-}2$ worth of CuSn catalysts electrodeposited

on carbon-based GDLs from a 1.53 M MSA electrolyte with a $[Cu^{2+}]/[Sn^{2+}]$ molar ratio of 1 at different current densities: (**A**) 10 mA cm^{-2}, (**B**) 20 mA cm^{-2}, (**C**) 30 mA cm^{-2}.

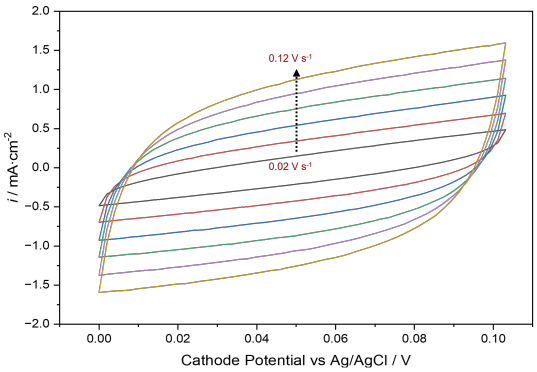


Figure A16. CVs conducted within a potential window of ±50 mV versus the OCP in 1 M KOH at scan rates of 20–120 mV s^{-1} over GDL with no catalyst after HNO_3 treatment.

References

1. Filonchyk, M.; Peterson, M.P.; Zhang, L.; Hurynovich, V.; He, Y. Greenhouse gases emissions and global climate change: Examining the influence of CO_2, CH_4, and N_2O. *Sci. Total Environ.* **2024**, *935*, 173359. [CrossRef] [PubMed]
2. Kiehbadroudinezhad, M.; Merabet, A.; Hosseinzadeh-Bandbafha, H. Chapter Twelve—Health impacts of greenhouse gases emissions on humans and the environment. In *Advances and Technology Development in Greenhouse Gases: Emission, Capture and Conversion*; Elsevier: Amsterdam, The Netherlands, 2024; Volume 935, pp. 265–291. [CrossRef]
3. Ofremu, G.O.; Raimi, B.Y.; Yusuf, S.O.; Dziwornu, B.A.; Nnabuife, S.G.; Eze, A.M.; Nnajiofor, C.A. Exploring the relationship between climate change, air pollutants and human health: Impacts, adaptation, and mitigation strategies. *Green Energy Resour.* **2025**, *3*, 2949–7205. [CrossRef]
4. Kumar, A.; Kumar, A.; Kumar, M.; Bhat, J.A. Greenhouse Gas Emissions and Terrestrial Ecosystems. *Front. Environ. Sci.* **2022**, *10*, 173359. [CrossRef]
5. Keeling, C.D.; Bacastow, R.B.; Bainbridge, C.A.; Guenther, P.R.; Waterman, L.S.; Chin, J.F.S. Atmospheric carbon dioxide variations at Mauna Loa Observatory, Hawaii. *Tellus* **1976**, *28*, 538–551. [CrossRef]
6. National Center for Environmental Information. A Paleo Perspective on Global Warming: Temperature Change and Carbon Dioxide Change. 2013. Available online: https://www.ncei.noaa.gov/sites/default/files/2021-11/8%20-%20Temperature%20Change%20and%20Carbon%20Dioxide%20Change%20-%20FINAL%20OCT%202021.pdf (accessed on 8 June 2025).
7. Lüthi, D.; Le Floch, M.; Bereiter, B.; Blunier, T.; Barnola, J.M.; Siegenthaler, U.; Raynaud, D.; Jouzel, J.; Fischer, H.; Kawamura, K.; et al. High-resolution carbon dioxide concentration record 650,000–800,000 years before present. *Nature* **2008**, *453*, 379–382. [CrossRef]
8. U.S. Environmental Protection Agency. Global Greenhouse Gas Emissions Overview. 2024. Available online: https://www.epa.gov/ghgemissions/global-greenhouse-gas-overview (accessed on 8 June 2025).
9. International Energy Agency. CO_2 Emissions in 2023: A New Record High, but Is There a Light at the End of the Tunnel? IEA, Paris. 2024. Available online: https://www.iea.org/reports/co2-emissions-in-2023 (accessed on 8 June 2025).
10. Davis, S.J.; Lewis, N.S.; Shaner, M.; Aggarwal, S.; Arent, D.; Azevedo, I.L.; Benson, S.M.; Bradley, T.; Brouwer, J.; Chiang, Y.-M.; et al. Net-Zero Emissions Energy Systems. *Science* **2018**, *360*, eaas9793. [CrossRef] [PubMed]
11. The Royal Society. *Catalysing Change: Defossilising the Chemical Industry—Policy Briefing*; The Royal Society: London, UK, 2024; ISBN 978-1-78252-705-3. Available online: https://royalsociety.org/-/media/policy/projects/defossilising-chemicals/defossilising-chemical-industry-report.pdf (accessed on 4 January 2026).
12. International Energy Agency. Clean Energy Market Monitor IEA, Paris. 2024. Available online: https://www.iea.org/reports/clean-energy-market-monitor-march-2024 (accessed on 8 June 2025).
13. Bauer, F.; Tilsted, J.P.; Pfister, S.; Oberschelp, C.; Kulionis, V. Mapping GHG emissions and prospects for renewable energy in the chemical industry. *Curr. Opin. Chem. Eng.* **2023**, *39*, 2211–3398. [CrossRef]
14. Worku, A.K.; Ayele, D.W.; Deepak, D.B.; Gebreyohannes, A.Y.; Agegnehu, S.D.; Kolhe, M.L. Recent Advances and Challenges of Hydrogen Production Technologies via Renewable Energy Sources. *Adv. Energy Sustain. Res.* **2024**, *5*, 2699–9412. [CrossRef]
15. Nurdiawati, A.; Urban, F. Towards Deep Decarbonisation of Energy-Intensive Industries: A Review of Current Status, Technologies and Policies. *Energies* **2021**, *14*, 2408. [CrossRef]
16. Nitopi, S.; Bertheussen, E.; Scott, B.S.; Liu, X.; Engstfeld, A.; Horch, S.; Seger, B.; Stephens, I.; Chan, K.; Hahn, C.; et al. Progress and Perspectives of Electrochemical CO_2 Reduction on Copper in Aqueous Electrolyte. *Chem. Rev.* **2019**, *119*, 7610–7672. [CrossRef]

17. Wang, R.; Assenova, V.A.; Hertwich, E.G. Energy System Decarbonization and Productivity Gains Reduced the Coupling of CO_2 Emissions and Economic Growth in 73 Countries between 1970 and 2016. *One Earth* **2021**, *4*, 1614–1624. [CrossRef]
18. Office for National Statistics. The Decoupling of Economic Growth from Carbon Emissions: UK Evidence. 2019. Available online: https://www.ons.gov.uk/economy/nationalaccounts/uksectoraccounts/compendium/economicreview/october2019/thedecouplingofeconomicgrowthfromcarbonemissionsukevidence (accessed on 8 June 2025).
19. Vega-Ortiz, C.; Silva-Arizabalo, J.R.; Salas-Solis, F.A.; Navarro-Tovar, L.G.; Jimenez-Viacobo, J.; Garza-Morales, E.M.; Lidia-Martinez, A.; Aguilera-Vazquez, L. Implementación de Sistemas de Captura de CO_2 en Yacimientos Geológicos en Tamaulipas. In Proceedings of the Congreso Mexicano del Petroleo, Tampico, Mexico, 20 June 2024; (CMP2024_507).
20. Hajiyev, E.; Watson, M.; Emadi, H.; Eissa, B.; Hussain, A.; Baig, A.R.; Shahin, A. A Comparative Study of Major Risk Assessment (RA) Frameworks in Geologic Carbon Storage (GCS). *Fuels* **2025**, *6*, 42. [CrossRef]
21. Bukar, A.M.; Asif, M. Technology Readiness Level Assessment of Carbon Capture and Storage Technologies. *Renew. Sustain. Energy Rev.* **2024**, *200*, 114578. [CrossRef]
22. Nwabueze, Q.A.; Leggett, S. Advancements in the Application of CO_2 Capture and Utilization Technologies—A Comprehensive Review. *Fuels* **2024**, *5*, 508–532. [CrossRef]
23. Wang, T.; Dong, C.D.; Lin, J.Y.; Chen, C.W.; Chang, J.S.; Kim, H.; Huang, C.P.; Hung, C.M. Recent Advances in Carbon Dioxide Conversion: A Circular Bioeconomy Perspective. *Sustainability* **2021**, *13*, 6962. [CrossRef]
24. National Academies of Sciences, Engineering, and Medicine. *Gaseous Carbon Waste Streams Utilization: Status and Research Needs*; The National Academies Press: Washington, DC, USA, 2019; pp. 39–41, 63–83. [CrossRef]
25. Owgi, A.H.K.; Jalil, A.A.; Hussain, I.; Hassan, N.S.; Hambali, H.U.; Siang, T.J.; Vo, D.V.N. Catalytic Systems for Enhanced Carbon Dioxide Reforming of Methane: A Review. *Environ. Chem. Lett.* **2021**, *19*, 2157–2183. [CrossRef]
26. Marques, L.; Vieira, M.; Condeço, J.; Henriques, C.; Mateus, M. A Mini-Review on Recent Developments and Improvements in CO_2 Catalytic Conversion to Methanol: Prospects for the Cement Plant Industry. *Energies* **2024**, *17*, 5285. [CrossRef]
27. Guil-López, R.; Mota, N.; Llorente, J.; Millán, E.; Pawelec, B.; Fierro, J.L.G.; Navarro, R.M. Methanol Synthesis from CO_2: A Review of the Latest Developments in Heterogeneous Catalysis. *Materials* **2019**, *12*, 3902. [CrossRef] [PubMed]
28. Navarro-Jaén, S.; Virginie, M.; Bonin, J.; Robert, M.; Wojcieszak, R.; Khodakov, A.Y. Highlights and Challenges in the Selective Reduction of Carbon Dioxide to Methanol. *Nat. Rev. Chem.* **2021**, *5*, 564–579. [CrossRef] [PubMed]
29. Ud Din, I.; Shaharun, M.S.; Alotaibi, M.A.; Alharthi, A.I.; Naeem, A. Recent Developments on Heterogeneous Catalytic CO_2 Reduction to Methanol. *J. CO_2 Util.* **2019**, *34*, 20–33. [CrossRef]
30. Xie, S.; Zhang, W.; Lan, X.; Lin, H. CO_2 Reduction to Methanol in the Liquid Phase: A Review. *ChemSusChem* **2020**, *13*, 6141–6159. [CrossRef]
31. Inoue, T.; Fujishima, A.; Konishi, S.; Honda, K. Photoelectrocatalytic Reduction of Carbon Dioxide in Aqueous Suspensions of Semiconductor Powders. *Nature* **1979**, *277*, 637–638. [CrossRef]
32. Habisreutinger, S.N.; Schmidt-Mende, L.; Stolarczyk, J.K. Photocatalytic Reduction of CO_2 on TiO_2 and Other Semiconductors. *Angew. Chem. Int. Ed.* **2013**, *52*, 7372–7408. [CrossRef]
33. Ferreira de Brito, J.; Bessegato, G.G.; Perini, J.A.L.; Torquato, L.D.D.M.; Zanoni, M.V.B. Advances in Photoelectroreduction of CO_2 to Hydrocarbon Fuels: Contributions of Functional Materials. *J. CO_2 Util.* **2022**, *55*, 101810. [CrossRef]
34. Shinde, G.Y.; Mote, A.S.; Gawande, M.B. Recent Advances of Photocatalytic Hydrogenation of CO_2 to Methanol. *Catalysts* **2022**, *12*, 94. [CrossRef]
35. Gupta, R.; Mishra, A.; Thirupathaiah, Y.; Chandel, A.K. Biochemical Conversion of CO_2 in Fuels and Chemicals: Status, Innovation, and Industrial Aspects. *Biomass Convers. Biorefinery* **2024**, *14*, 3007–3030. [CrossRef]
36. Stephens, S.; Mahadevan, R.; Allen, D.G. Engineering Photosynthetic Bioprocesses for Sustainable Chemical Production: A Review. *Front. Bioeng. Biotechnol.* **2021**, *8*, 610723. [CrossRef] [PubMed]
37. Karishma, S.; Kamalesh, R.; Saravanan, A.; Deivayanai, V.C.; Yaashikaa, P.R.; Vickram, A.S. A Review on Recent Advancements in Biochemical Fixation and Transformation of CO_2 into Constructive Products. *Biochem. Eng. J.* **2024**, *208*, 109366. [CrossRef]
38. Tovar-Oliva, M.S.; Tandava, V.S.R.K.; Bößl, F.; Menzel, V.C.; Zarco-Roldán, J.A.; Rae, R.; Kirk, C.; Murcia-López, S.; Tudela, I. Importance of Optimising Electrodeposition Parameters for Scalable and Cost-Effective Manufacturing of Cu Catalysts for Efficient Electrochemical CO_2 Reduction to Renewable Fuels and Chemical Feedstocks. *Mater. Today Sustain.* **2025**, *31*, 101116. [CrossRef]
39. Li, Y.C. The Road to the Electroreduction of CO_2. *Commun. Chem.* **2024**, *7*, 48. [CrossRef]
40. Leonzio, G.; Hankin, A.; Shah, N. CO_2 Electrochemical Reduction: A State-of-the-Art Review with Economic and Environmental Analyses. *Chem. Eng. Res. Des.* **2024**, *208*, 934–955. [CrossRef]

41. Tandava, V.S.R.K.; Tovar-Oliva, M.S.; Biset-Peiró, M.; Sylla, D.; Morante, J.R.; Tudela, I.; Murcia-López, S. Modulating the Surface Interface of PTFE/Cu-Based GDEs to Boost the Electrochemical Conversion of CO_2 to C_2H_4 at Ultra-Low Overpotential. *Appl. Catal. B Environ. Energy* **2025**, *371*, 125276. [CrossRef]
42. Yao, Y.; Shi, T.; Chen, W.; Wu, J.; Fan, Y.; Liu, Y.; Cao, L.; Chen, Z. A Surface Strategy Boosting the Ethylene Selectivity for CO_2 Reduction and In Situ Mechanistic Insights. *Nat. Commun.* **2024**, *15*, 1257. [CrossRef]
43. Lu, T.; Xu, T.; Zhu, S.; Li, J.; Wang, J.; Jin, H.; Wang, X.; Lv, J.-J.; Wang, Z.-J.; Wang, S. Electrocatalytic CO_2 Reduction to Ethylene: From Advanced Catalyst Design to Industrial Applications. *Adv. Mater.* **2023**, *35*, 2310433. [CrossRef]
44. Li, F.; Thevenon, A.; Rosas-Hernández, A.; Wang, Z.; Li, Y.; Gabardo, C.M.; Ozden, A.; Dinh, C.T.; Li, J.; Wang, Y.; et al. Molecular Tuning of CO_2-to-Ethylene Conversion. *Nature* **2020**, *577*, 509–513. [CrossRef] [PubMed]
45. Ye, K.; Cao, A.; Shao, J.; Wang, G.; Si, R.; Ta, N.; Xiao, J.; Wang, G. Synergy Effects on Sn-Cu Alloy Catalyst for Efficient CO_2 Electroreduction to Formate with High Mass Activity. *Sci. Bull.* **2020**, *65*, 711–719. [CrossRef]
46. Kortlever, R.; Peters, I.; Koper, S.; Koper, M.T.M. Electrochemical CO_2 Reduction to Formic Acid at Low Overpotential and with High Faradaic Efficiency on Carbon-Supported Bimetallic Pd–Pt Nanoparticles. *ACS Catal.* **2015**, *5*, 3916–3923. [CrossRef]
47. Morimoto, M.; Takatsuji, Y.; Yamasaki, R.; Hashimoto, H.; Nakata, I.; Sakakura, T.; Haruyama, T. Electrodeposited Cu-Sn Alloy for Electrochemical CO_2 Reduction to $CO/HCOO^-$. *Electrocatalysis* **2018**, *9*, 323–332. [CrossRef]
48. Varela, H.; Paredes-Salazar, E.A.; Lima, F.H.B.; Eid, K. Renewable Methanol and the Energy Challenge: The Role of Electrocatalysis. *Curr. Opin. Electrochem.* **2024**, *46*, 101539. [CrossRef]
49. Liu, Y.; Li, F.; Zhang, X.; Ji, X. Recent Progress on Electrochemical Reduction of CO_2 to Methanol. *Curr. Opin. Green Sustain. Chem.* **2020**, *23*, 10–17. [CrossRef]
50. Wiranarongkorn, K.; Eamsiri, K.; Chen, Y.-S.; Arpornwichanop, A. A Comprehensive Review of Electrochemical Reduction of CO_2 to Methanol: Technical and Design Aspects. *J. CO_2 Util.* **2023**, *71*, 102477. [CrossRef]
51. Alkoshab, M.Q.; Thomou, E.; Abdulazeez, I.; Suliman, M.H.; Spyrou, K.; Iali, W.; Alhooshani, K.; Baroud, T.N. Low Overpotential Electrochemical Reduction of CO_2 to Ethanol Enabled by Cu/Cu_xO Nanoparticles Embedded in Nitrogen-Doped Carbon Cuboids. *Nanomaterials* **2023**, *13*, 230. [CrossRef]
52. Ke, X.; Xu, W.; Liu, C.; Wang, Y.; Huang, X.; Xiao, R.; Xu, X.; Li, T.; Shao, Z. Innovative Electrode Designs for Low-Temperature Electrochemical CO_2 Reduction with Ampere-Level Performance. *Energy Environ. Sci.* **2025**, *18*, 7792–7858. [CrossRef]
53. Chen, C.; Khosrowabadi Kotyk, J.F.; Sheehan, S.W. Progress toward Commercial Application of Electrochemical Carbon Dioxide Reduction. *Chem* **2018**, *4*, 2571–2586. [CrossRef]
54. London Metal Exchange (LME). LME Tin Prices—July 2025. Available online: https://www.lme.com/en/metals/non-ferrous/lme-tin (accessed on 31 July 2025).
55. Trading Economics. Indium Price. Available online: https://tradingeconomics.com/commodity/indium (accessed on 31 July 2025).
56. Metal.com. Bismuth Prices. Available online: https://www.metal.com/Bismuth-Selenium-Tellurium/202212020004 (accessed on 31 July 2025).
57. Lei, T.; Zhang, X.; Jung, J.; Cai, Y.; Hou, X.; Zhang, Q.; Qiao, J. Continuous Electroreduction of Carbon Dioxide to Formate on Tin Nanoelectrode Using Alkaline Membrane Cell Configuration in Aqueous Medium. *Catal. Today* **2017**, *318*, 32–38. [CrossRef]
58. Chang, F.; Xiao, M.; Miao, R.; Ma, L.; Hu, C.; Chen, R.; Wang, J.; Sun, X. Copper-Based Catalysts for Electrochemical Carbon Dioxide Reduction to Multicarbon Products. *Electrochem. Energy Rev.* **2022**, *5*, 4. [CrossRef]
59. Xie, L.; Jiang, Y.; Zhu, W.; Ding, S.; Zhou, Y.; Zhu, J. Cu-based catalyst designs in CO_2 electroreduction: Precise modulation of reaction intermediates for high-value chemical generation. *Chem. Sci.* **2023**, *14*, 13629–13660. [CrossRef]
60. Bagger, A.; Ju, W.; Varela, A.S.; Strasser, P.; Rossmeisl, J. Electrochemical CO_2 Reduction: A Classification Problem. *ChemPhysChem* **2017**, *18*, 3266–3273. [CrossRef]
61. El–Nagar, G.A.; Yang, F.; Stojkovikj, S.; Mebs, S.; Gupta, S.; Ahmet, I.Y.; Dau, H.; Mayer, M.T. Comparative Spectroscopic Study Revealing Why the CO_2 Electroreduction Selectivity Switches from CO to $HCOO^-$ at Cu–Sn- and Cu–In-Based Catalysts. *ACS Catal.* **2022**, *12*, 15576–15589. [CrossRef] [PubMed]
62. Shen, H.; Jin, H.; Li, H.; Wang, Z.; Lu, S.; Ma, S.; Zhang, S.; Yang, H.; Zhang, X. Acidic CO_2-to-HCOOH Electrolysis with Industrial-Level Current on Phase-Engineered Tin Sulfide. *Nat. Commun.* **2023**, *14*, 2843. [CrossRef]
63. Tabassum, H.; Yang, X.; Zou, R.; Wu, G. Surface engineering of Cu catalysts for electrochemical reduction of CO_2 to value-added multi-carbon products. *Chem Catal.* **2022**, *2*, 1561–1593. [CrossRef]
64. Al Harthi, A.; Al Abri, M.; Younus, H.A.; Al Hajri, R. Criteria and cutting-edge catalysts for CO_2 electrochemical reduction at the industrial scale. *J. CO_2 Util.* **2024**, *83*, 102819. [CrossRef]

65. Deng, X.; Alfonso, D.; Nguyen-Phan, T.-D.; Kauffman, D.R. Resolving the Size-Dependent Transition between CO_2 Reduction Reaction and H_2 Evolution Reaction Selectivity in Sub-5 nm Silver Nanoparticle Electrocatalysts. *ACS Catal.* **2022**, *12*, 5921–5929. [CrossRef]
66. Tovar-Oliva, M.S.; Tudela, I. Electrodeposition of Nano- and Micro-Materials: Advancements in Electrocatalysts for Electrochemical Applications. *Results Eng.* **2024**, *24*, 103285. [CrossRef]
67. Jhong, H.-R.M.; Brushett, F.R.; Kenis, P.J.A. The Effects of Catalyst Layer Deposition Methodology on Electrode Performance. *Adv. Energy Mater.* **2013**, *3*, 589–599. [CrossRef]
68. Hoang, T.T.H.; Ma, S.; Gold, J.I.; Kenis, P.J.A.; Gewirth, A.A. Nanoporous Copper Films by Additive-Controlled Electrodeposition: CO_2 Reduction Catalysis. *ACS Catal.* **2017**, *7*, 3313–3321. [CrossRef]
69. Hoang, T.T.H.; Verma, S.; Ma, S.; Fister, T.T.; Timoshenko, J.; Frenkel, A.I.; Kenis, P.J.A.; Gewirth, A.A. Nanoporous Copper–Silver Alloys by Additive-Controlled Electrodeposition for the Selective Electroreduction of CO_2 to Ethylene and Ethanol. *J. Am. Chem. Soc.* **2018**, *140*, 5791–5797. [CrossRef] [PubMed]
70. Low, C.T.J.; Walsh, F.C. Electrodeposition of Tin, Copper and Tin–Copper Alloys from a Methanesulfonic Acid Electrolyte Containing a Perfluorinated Cationic Surfactant. *Surf. Coat. Technol.* **2008**, *202*, 1339–1349. [CrossRef]
71. Zanella, C.; Xing, S.; Deflorian, F. Effect of Electrodeposition Parameters on Chemical and Morphological Characteristics of Cu–Sn Coatings from a Methanesulfonic Acid Electrolyte. *Surf. Coat. Technol.* **2013**, *236*, 394–399. [CrossRef]
72. Walsh, F.C.; Low, C.T.J. A Review of Developments in the Electrodeposition of Tin–Copper Alloys. *Surf. Coat. Technol.* **2016**, *304*, 246–262. [CrossRef]
73. Li, D.; Xie, S.; Liang, J.; Ma, B.; Fu, J.; Wu, J.; Feng, Y.; Feng, Z. Structure Regulated CuSn Alloy Catalyst for Selective Electrochemical CO_2-to-Formate Conversion at Higher Current Densities. *Sep. Purif. Technol.* **2024**, *340*, 126545. [CrossRef]
74. Popov, K.I.; Sjokić, S.S.; Grgur, B.N. *Fundamental Aspects of Electrometallurgy*; Kluwer Academic Publishers: New York, NY, USA, 2002. [CrossRef]
75. Gernon, M.D.; Wu, M.; Buszta, T.; Janney, P. Environmental benefits of methanesulfonic acid: Comparative properties and advantages. *Green Chem.* **1999**, *1*, 127–140. [CrossRef]
76. Binnemans, K.; Jones, P.T. Methanesulfonic Acid (MSA) in Hydrometallurgy. *J. Sustain. Metall.* **2023**, *9*, 26–45. [CrossRef]
77. Perry, S.C.; Ponce de León, C.; Walsh, F.C. Review—The Design, Performance and Continuing Development of Electrochemical Reactors for Clean Electrosynthesis. *J. Electrochem. Soc.* **2020**, *167*, 155525. [CrossRef]
78. Bengoa, L.N.; Pary, P.; Conconi, M.S.; Egli, W.A. Electrodeposition of Cu–Sn alloys from a methanesulfonic acid electrolyte containing benzyl alcohol. *Electrochim. Acta* **2017**, *256*, 211–219. [CrossRef]
79. Zarrouk, A.; Hammouti, B.; Al-Deyab, S.S.; Salghi, R.; Zarrok, H.; Jama, C.; Bentiss, F. Corrosion inhibition performance of 3,5-diamino-1,2,4-triazole for protection of copper in nitric acid solution. *Int. J. Electrochem. Sci.* **2012**, *7*, 5997–6011. [CrossRef]
80. Gražulis, S.; Chateigner, D.; Downs, R.T.; Yokochi, A.F.T.; Quirós, M.; Lutterotti, L.; Manakova, E.; Butkus, J.; Moeck, P.; Le Bail, A. Crystallography open database—An open-access collection of crystal structures. *J. Appl. Crystallogr.* **2009**, *42*, 726–729. [CrossRef]
81. Trasatti, S.; Petrii, O.A. Real Surface Area Measurements in Electrochemistry. *Pure Appl. Chem.* **1991**, *63*, 711–734. [CrossRef]
82. Nekouei, R.K.; Mofarah, S.S.; Maroufi, S.; Tudela, I.; Sahajwalla, V. Determination of the Optimum Potential Window for Super- and Pseudocapacitance Electrodes via In-Depth Electrochemical Impedance Spectroscopy Analysis. *J. Energy Storage* **2022**, *56*, 106137. [CrossRef]
83. Schouten, K.J.P.; Qin, Z.; Pérez Gallent, E.; Koper, M.T.M. Two pathways for the formation of ethylene in CO reduction on single-crystal copper electrodes. *J. Am. Chem. Soc.* **2012**, *134*, 9864–9867. [CrossRef] [PubMed]
84. Luo, W.; Nie, X.; Janik, M.J.; Asthagiri, A. Facet dependence of CO_2 reduction paths on Cu electrodes. *ACS Catal.* **2016**, *6*, 219–229. [CrossRef]
85. Xu, Y.; Zhang, L. A First-Principles Study on the Reaction Mechanisms of Electrochemical CO_2 Reduction to C_1 and C_2 Products on Cu(110). *Catalysts* **2024**, *14*, 468. [CrossRef]
86. Huang, J.; Zhang, X.; Yang, J.; Yu, J.; Chen, Q.; Peng, L. Recent Progress on Copper-Based Bimetallic Heterojunction Catalysts for CO_2 Electrocatalysis: Unlocking the Mystery of Product Selectivity. *Adv. Sci.* **2024**, *11*, e2309865. [CrossRef]
87. Liu, M.; Wang, Q.; Luo, T.; Herran, M.; Cao, X.; Liao, W.; Zhu, L.; Li, H.; Stefancu, A.; Lu, Y.R.; et al. Potential Alignment in Tandem Catalysts Enhances CO_2-to-C_2H_4 Conversion Efficiencies. *J. Am. Chem. Soc.* **2024**, *146*, 468–475. [CrossRef]
88. Cook, R.L.; MacDuff, R.C.; Sammells, A.F. Evidence for Formaldehyde, Formic Acid, and Acetaldehyde as Possible Intermediates during Electrochemical Carbon Dioxide Reduction at Copper. *J. Electrochem. Soc.* **1989**, *136*, 1982. [CrossRef]
89. Ko, Y.J.; Kim, J.Y.; Lee, W.H.; Kim, M.G.; Seong, T.; Park, J.; Jeong, Y.; Min, B.K.; Lee, W.; Lee, D.K.; Oh, H.S. Exploring Dopant Effects in Stannic Oxide Nanoparticles for CO_2 Electro-Reduction to Formate. *Nat. Commun.* **2022**, *13*, 2205. [CrossRef]
90. Wang, T.; Chen, J.; Ren, X.; Zhang, J.; Ding, J.; Liu, Y.; Lim, K.H.; Wang, J.; Li, X.; Yang, H.; et al. Halogen-Incorporated Sn Catalysts for Selective Electrochemical CO_2 Reduction to Formate. *Angew. Chem. Int. Ed.* **2023**, *62*, e202211174. [CrossRef]
91. Arabsahebi, A.; Akbarian, P.; Kheirmand, M. Carbon fiber paper based on composites of carbon and polyacrylonitrile for fuel cell application. *Carbon Trends* **2024**, *14*, 100335. [CrossRef]

92. Chen, Q.; Niu, Z.; Li, H.; Jiao, K.; Wang, Y. Recent progress of gas diffusion layer in proton exchange membrane fuel cell: Two-phase flow and material properties. *Int. J. Hydrogen Energy* **2021**, *46*, 8640–8671. [CrossRef]
93. Zanellato, G.; Schiavi, P.; Rubino, A.; Altimari, P.; Pagnanelli, F. Electrochemical Pretreatments of Carbon Paper and Their Effect on the Electrodeposition of Metallic Nanostructures. *Chem. Eng. Trans.* **2021**, *84*, 115–120. [CrossRef]

Disclaimer/Publisher's Note: The statements, opinions and data contained in all publications are solely those of the individual author(s) and contributor(s) and not of MDPI and/or the editor(s). MDPI and/or the editor(s) disclaim responsibility for any injury to people or property resulting from any ideas, methods, instructions or products referred to in the content.